Electron and Nuclear Spin Dynamics in n-GaAs

Von der Fakultät für Mathematik und Physik

der Gottfried Wilhelm Leibniz Universität Hannover

zur Erlangung des Grades

Doktorin der Naturwissenschaften

Dr. rer. nat.

genehmigte Dissertation

von

M.Sc. Lida Abaspour

2021

Referent: Prof. Dr. M. Oestreich
Leibniz Universität Hannover

Korreferent: Prof. Dr. F. Ding
Leibniz Universität Hannover

Korreferent: Prof. Dr. T. Korn
Universität Rostock

Tag der Promotion: 19.10.2021

Abstract

The spin degree of freedom of charge carrier spins and the host's nuclear spins in semiconductors are potential sources for the next generation of spintronics applications which motivate the deliberate investigation of the spin dynamics of well-controlled model systems like n-GaAs. Conduction electron spins are mobile in semiconductors and can be initialized, manipulated, and read out optically. Optical pumping with circularly polarized light can for example create a non-equilibrium electron spin polarization close to 100%. Nuclear spins are practically appealing as well due to their very long spin relaxation times. The mutual interaction between the electron and nuclear spin system is mediated via the hyperfine interaction. Indeed, through this interaction, a non-equilibrium spin polarization of electrons is transferred to the nuclear spins and results in dynamic nuclear polarization, which *inter alia* has an intricate dependence on the doping density. The main objectives of this thesis are measuring most accurately (i) the temperature dependence of the electron spin relaxation rate and (ii) the magnetic field, doping, and temperature dependence of the nuclear spin relaxation rate in a set of high quality n-GaAs samples from quasi-insulating over the metal-to-insulator transition up to the quasimetallic regime.

The temperature dependence of the electron spin relaxation time is measured very accurately for three of the above-mentioned samples with the optical Hanle depolarization method. The measurements yield, in combination with a theoretical model, a quantitative insight into the efficiency of the different spin relaxation mechanisms. The longest electron spin relaxation time in n-GaAs results from an interplay of variable range hopping and hyperfine interaction for a doping concentration just below the Mott metal-to-insulator transition at a finite temperature of ~ 7 K. At higher

doping densities the effect of these two mechanisms decreases such that they are negligible in the highest doped sample. For moderate and high temperatures, the description of the electron spin relaxation becomes unpretentious since the Dyakonov-Perel mechanism dominates over all other electron spin relaxation mechanisms.

The Overhauser field from nuclear polarization intensifies or weakens the external magnetic field and affects the electron spin orientation. In order to measure the nuclear spin relaxation, a three-stage time-resolved detection of the Hanle effect is used. The method includes optical pumping and measuring the difference of the nuclear spin polarization before and after a dark (no laser light) interval of variable length. In this way, the nuclear spin system in the absence of excitation is investigated. The magnetic field dependence of the nuclear spin relaxation rate has a typical Lorentzian shape, showing the spin-spin interaction's impact at lower magnetic fields. The strong field doping dependence of the nuclear spin relaxation rate can be explained *quantitatively*, considering the effective number of localized electrons over the entire density regime. Nuclear spin diffusion to the donor bound electrons increases the relaxation rate of the nuclear spin measured at 6.5 K and results in a distinct maximum at the metal-to-insulator transition. The rate in the very high doped sample increases due to the Korringa mechanism. The involved mechanisms explain the trend of the relaxation except for the very low doped sample. The temperature dependence of the lowest doped sample shows an electron spin relaxation channel affecting the nuclear spin relaxation, which is negligible at high doping densities.

4

Contents

List of Abbreviations, Symbols, and Constants

Abbreviations

DDI Dipole-Dipole Interaction

DNP Dynamic Nuclear Polarization

DP Dyakonov-Perel

ESR Electron Spin Relaxation

FR Faraday Rotation

FD Fermi-Dirac

GaAs Gallium Arsenide

Hanle Hanle Method

HFI Hyperfine Interaction

HWHM Half Width at Half Maximum

KF Knight Field

LP linear polarizer

MIT Metal-to-Insulator Transition

NMR Nuclear Magnetic Resonance

NSR Nuclear Spin Relaxation

OF Overhauser Field

PEM Photoelastic Modulator

PL Photoluminescence

QPI Quadrupole Interaction

Si Silicon

SOI Spin Orbit Interaction

VRH Variable Range Hopping

Symbols

τ_c correlation time

θ_D Debye temperature

γ_D Dresselhaus constant

n_d doping density

m_e^* effective electron mass

ω_e electron Larmor frequency

g_e electron g-factor

$\tau_{s,\,DP}^{-1}$ electron spin relaxation due to Dyakonov-Perel mechanism

$\tau_{s,\,HFI}^{-1}$ electron spin relaxation due to hyperfine interaction

$\tau_{s,\,VRH}^{-1}$ electron spin relaxation due to variable range hopping

τ_s electron spin relaxation time

E_g energy gap

B_{ext} external magnetic field

ζ Fermi-Boltzmann factor

f_{FD} Fermi-Dirac distribution

E_F Fermi energy

γ_e gyromagnetic ratio of electron

γ_n gyromagnetic ratio of nuclear

n_H charge carrier concentration determined from the Hall resistance

A_{HF} hyperfine coupling constant

B_e Knight field

ω_L Larmor frequency

a lattice constant

B_L local field

f_{MB} Maxwell-Boltzmann distribution

τ_p momentum relaxation time

ω_n nuclear Larmor frequency

B_N nuclear magnetic field

D_{av} nuclear spin diffusion coefficient

g_n nuclear g-factor

Γ_{ESR} nuclear spin relaxation rate due to electron spin relaxation

Γ_K nuclear spin relaxation rate due to Korringa mechanism

Γ_P nuclear spin relaxation rate due to phonon interaction

Γ_D nuclear spin relaxation rate due to spin diffusion

Γ_Z nuclear spin relaxation rate due to Zeeman interaction

θ_N nuclear spin temperature

R_{opt} optimal hopping distance

γ_3 proportionality factor between τ_c and τ_p

ξ the ratio of Γ_{ss} and Γ_Z

ϵ_r relative permittivity

D_{hop} specific diffusion constant

T_1 spin relaxation time

T_2 spin dephasing time

Γ_{ss} spin-spin relaxation rate

T temperature

Constants

μ_B Bohr magneton, $9.274\,009\,994 \times 10^{-24}\,\mathrm{J\,T^{-1}}$

a_B Bohr radius, $5.291\,772\,109\,03(80) \times 10^{-11}\,\mathrm{m}$

k_B Boltzmann constant, $1.380\,648\,52 \times 10^{-23}\,\mathrm{J\,K^{-1}}$

m_e electron mass, $9.109\,389\,7 \times 10^{-31}\,\mathrm{kg}$

e elementary charge, $1.602\,176\,62 \times 10^{-19}\,\mathrm{C}$

μ_N nuclear magneton, $5.050\,783\,699(31) \times 10^{-27}\,\mathrm{J\,T^{-1}}$

h Planck constant, $6.626\,070\,040 \times 10^{-34}\,\mathrm{J\,s}$

$\hbar$ reduced Planck constant, $1.054\,571\,800 \times 10^{-34}\,\mathrm{J\,s}$

m_p proton mass, $1.672\,623\,1 \times 10^{-27}\,\mathrm{kg}$

μ_0 vacuum permeability, $4\pi \times 10^{-7}\,\mathrm{H/m}$

ϵ_0 vacuum permittivity, $8.854\,187\,812\,8(13) \times 10^{-12}\,\mathrm{F/m}$

1. Introduction & Motivation

Since the use of transistors in the 1940s, semiconductor components have been of great importance in electronic devices. The development of integrated circuits led to the development of computers based on solid-state circuits at a rapid rate. This advancement has improved the way of storing, accessing, and processing data. Simulation and computer modeling facilitate the calculation of analytically intractable problems.

In 1965 the co-founder and chairman of Intel Corporation, Gordon Moore, wrote an article for the Electronics Magazine. He posited that the number of components of integrated circuits (including transistors, resistors, diodes, and capacitors) double roughly every year. Later, he revised his prediction to a doubling every 18 months [1]. Since then, Moore's law has remained valid. However, nowadays semiconductor technology progress faces fundamental obstacles. Technology approaches the limits of miniaturization and the performance of traditional transistors. Thus, new ways of processing information are required.

Spintronics serves as a promising candidate to solve this problem by taking advantage of the electron spin instead of the electron charge [2, 3]. Spin-based devices operate in principle faster than charge-based ones. Moreover, spins can be polarized by different methods like optical orientation, spin injection, and also applying a magnetic field. The heat dissipation problem in charge-based integrated circuits is less significant in spin-based ones. Thus, trying to solve the problem of putting more components into one circuit is accompanied by building new devices with lower energy consumption and dissipation. Beyond these applications based on traditional bits, spins offer an ideal two-level system for more advanced computer generations: quantum computers. Instead of binary logic, the

coherent superposition of the quantum mechanical states gives new opportunities to serve as quantum bits, the so-called qubits [4].

All of these advances in solid-state-based devices have been pretty established over the years by a series of ongoing profound and broader studies in some conventional semiconductors like silicon (Si) [5] and gallium arsenide (GaAs) [6]. The indirect bandgap is a big challenge in the optical applications of Si. GaAs is another option for these components. The direct bandgap of GaAs brings about efficiency in absorbing and emitting light and better optical performance, like in light-emitting diodes, lasers, and detectors [6]. Furthermore, most optical, electronic, and physical properties of GaAs are well studied in the literature. As a matter of concern, the spin dynamics in GaAs has been a main topic of research for over half a century and different experimental methods have been applied along the way [7–9], but there are still several open questions on electron and nuclear spin relaxation. In this dissertation, the spin dynamics of electron and nuclear spins in n-GaAs are investigated for doping densities from the quasi-insulating over the Mott metal-to-insulator transition (MIT) up to the quasimetallic regime. In order to explain the measurement results *quantitatively*, some of the parameters from auxiliary transport measurement on the same samples [10] are used.

Optical orientation, a process in which optical excitation with circularly polarized light excites spin polarized carriers, was first explained theoretically [11–13] and applied on semiconductors like Si [14], p-GaSb [15], p-AlGaAs [16], and p-GaAs [17]. Later, the experiments were done on n-type semiconductors by measuring the depolarization of the photoluminescence (PL) in a transverse magnetic field [12, 16, 18, 19]. This method known as Hanle effect was applied to measure the electron spin lifetime [19–21]. Other optical methods to measure the electron spin lifetime are for example Faraday rotation (FR) [22,23] and spin noise spectroscopy [24]. The effect of parameters such as doping and temperature on the electron spin relaxation (ESR) is in any semiconductor system of particular importance. In 2002, Dzhioev *et al.* measured the ESR rate on a range of doping densities in n-GaAs from $n_d = 1 \times 10^{14}$ cm^{-3} to $n_d = 5 \times 10^{17}$ cm^{-3} [25,26] at low temperature. The measured dop-

ing dependency of the ESR rate shows a minimum close to the MIT and implies different dominant spin relaxation mechanisms in different doping regimes. To clarify the involved relaxation mechanisms of ESR at the MIT, recently a series of optical and magneto-transport measurements have been performed on a wide range of n-GaAs by Lonnemann *et al.* [27]. The result provides at one single temperature a complete *quantitative* explanation of the involved scattering processes, which agrees with the experimentally measured ESR rate. To better understand the longest relaxation time in this set of samples, the temperature dependence of three of these samples is measured in this thesis. The result shows that the ESR rate in the sample below the MIT has a more pronounced temperature dependence in the whole measured temperature range. The interplay of the hyperfine interaction (HFI) and the variable range hopping (VRH) in this sample results in the lowest ever measured ESR rate in n-GaAs structures. The effect of the HFI and the VRH decreases above the MIT as the doping density increases, such that there is no significant effect of these two mechanisms at any temperature in the highest doped sample. At high temperatures, the Dyakonov-Perel (DP) mechanism dominates in all three samples as expected.

In addition to the electron spin system, the lattice nuclei possess spin angular momentum with weak coupling to the environment, emphasizing their potential importance for information storage. The coupling between electron and nuclear spin systems via HFI results in dynamic nuclear polarization (DNP) [28–32] which was first suggested by Overhauser in 1953 [33]. In this process, the lattice nuclei polarize via the interaction with the optically oriented electrons. Lampel was the first to observe the effect of the DNP on n-Si with nuclear magnetic resonance (NMR) [14]. Using luminescence depolarization of the electron spin system via Hanle effect, Paget *et al.* [34] measured the effect of small external magnetic field on the electron-nuclear spin coupling in p-GaAs. Later, they studied the relaxation of nuclei close to shallow donors via NMR [35]. The effect of delocalized electrons on the nuclear polarization was for example highlighted by Kikkawa *et al.* [22]. The effect of external factors on the NSR was also investigated. The dop-

ing dependence of the nuclear polarization via NMR was observed in
n-GaAs [36, 37]. The linear dependency of the NSR rate with tem-
perature was attributed to the Korringa mechanism [36, 38] which is
not valid anymore for very low temperatures in n-GaAs [39]. In all
of the proposed methods to measure the NSR including NMR, trans-
port, and optical measurements, the presence of the spin-polarized
electrons provide feedback that may change the behavior of the nu-
clear spins. Applying a three-stage time-resolved technique to mea-
sure the NSR rate in the absence of nonequilibrium electron spins
solves this problem [40–47]. In this method, the nuclei are polar-
ized in the presence of polarized electrons in the first bright stage.
A dark section follows where the NSR happens without optical ex-
citation, and the remaining nuclear spin polarization is measured
in a subsequent bright stage. This method - as a non-destructive
detection - is used in this thesis to measure the NSR rate in a set
of n-GaAs samples. The rate measured at 6.5 K increases in the
quasi-insulating regime with doping density due to nuclear spin dif-
fusion to the donor electrons and shows a distinct maximum at the
critical density of the MIT. The density dependence of the NSR
rate can be quantitatively calculated over the whole density regime
taking into account the effective number of localized electrons and
the interaction of free electrons via the Korringa mechanism. Only
the NSR rate of the very lowest doped sample shows a significant
deviation from these calculations.

This thesis is organized as follows: Chapter 2 outlines the electron-
nuclear spin system as an interconnected system. Both systems and
the underlying physical features are separately explained in this
chapter. The details of the experimental setup to create, manip-
ulate, and detect the spin polarization are presented in chapter 3.
For measuring the ESR, the Hanle method with no nuclear spin
involvement is used. In the presence of nuclear spin polarization,
a shift of the Hanle curve occurs, named as "oblique Hanle" in
this thesis. Both Hanle and oblique Hanle are explained in chap-
ter 3. The procedures for measuring both the ESR and the NSR
are also completely described in this chapter. Chapter 4 presents
the measurement results with the corresponding theoretical analy-

sis regarding the ESR and the NSR in two parts. In part I, the temperature-dependence of the ESR and the involved spin relaxation mechanisms including DP, VRH, and HFI are explained. The results for the NSR are provided in part II. Magnetic field dependence of the NSR is explained in section 4.8. The doping dependence of the NSR for the strong field range is discussed in section 4.9 along with the involved mechanisms. The temperature-dependence of the NSR for the lowest doped sample suggests, in this case, an additional NSR channel linked to the ESR rate, explained in section 4.10. Finally, chapter 5 summarizes this work and points out possible future measurements.

2. Fundamental Concepts

The electron and the lattice nuclei of GaAs have spin angular momentum and interact with each other. The coupling of the electron spin system with the nuclear spin system leads to different phenomena. This chapter provides theoretical background on the phenomena related to these systems. Section 2.1 gives a short overview of the general mutual interaction between the electron and the nuclear spin system. The nuclear spin system in GaAs is explained in detail in section 2.2. This section includes in particular two main interactions among nuclei, namely, dipole-dipole interaction (DDI) and quadrupole interaction (QPI). An explanation of the concept of the local field B_L, the spin temperature θ_N, and the Zeeman effect are provided as well. Section 2.3 explains the hyperfine interaction (HFI) by coupling between electron and nuclear spins. In this section, the induced Knight field (KF) from electron spins and the Overhauser field (OF) from nuclear spins as the static part of the HFI are summarized. The dynamic nuclear polarization (DNP) is discussed extensively in the last section of this chapter.

2.1. Electron-Nuclear Spin System

In a direct bandgap semiconductor, the generation of electron-hole pairs via absorbing photons is very efficient. Therefore, the interaction of circularly polarized light with a direct bandgap III-V semiconductor formed in a zinc blende crystal structure like GaAs is of great importance. In this process, the electron excitation into the conduction band is accompanied by leaving behind a hole in the valence band. Considering the momentum conservation, the angular momentum of the absorbed photon equals the change of the total
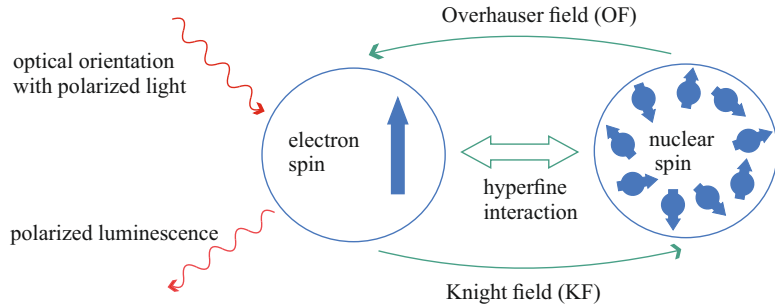
Figure 2.1.: Schematic illustration of the electron-nuclear spin system, optical orientation process, and transfer of spin from polarized electrons to nuclei via HFI. The fields experienced by the electron and nuclear spins via their counterpart, OF and KF, are also shown. The blue arrows indicate the spin in each group. The wiggly red arrows depict the incoming light and the polarized luminescence.

angular momentum of the electron and hole. The distribution of the spin angular momentum among them is based on the optical selection rules. With this interband absorption of light, a nonequilibrium electron spin system can be created. Afterwards, the spin angular momentum of this electron spin polarization can be transferred to the nuclei via HFI, and a nuclear polarization arises. Figure 2.1 demonstrates the coupled electron-nuclear spin system and the interaction processes among them.

The underlying mutual interaction among the systems, the HFI, plays an essential role in spin polarization and spin relaxation in bulk semiconductors and semiconductor nanostructures. The nuclear spins, polarized by the electron spin, act back via an effective magnetic field, known as Overhauser field (OF), and change the electron spin precession. The nuclear polarization depends on the electron spin polarization, which itself depends on the external field. Investigating the degree of the circular polarization of the PL from the electron-hole recombination provides information about this mu-

tual interaction.

2.2. Nuclear Spin System in GaAs

A nucleus with integer spin results from an even number of nucleons, while an odd number of nucleons yields a half-integer spin nucleus. All stable isotopes of GaAs (^{71}Ga, ^{69}Ga, ^{75}As) have spin 3/2. The relevant properties are summarized in Tab. 2.1 together with their natural abundances. Figure 2.2 schematically depicts the isotopes in GaAs with their possible spin orientations as small gray arrows. The spin of the donor-bound electrons is illustrated by thick black arrows and the electron wave function unscaled as shaded areas.
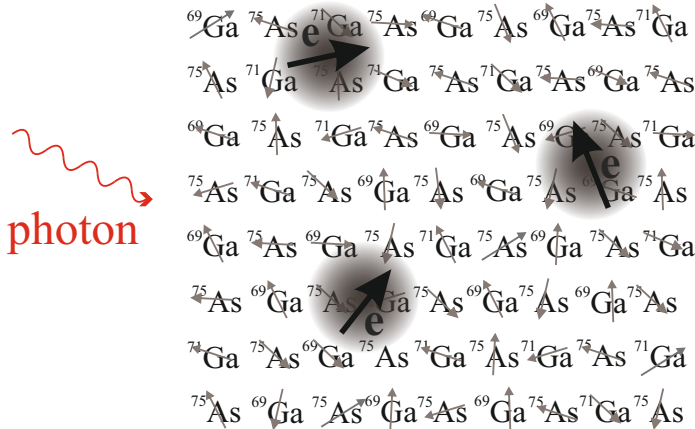
Figure 2.2.: An illustration of different isotopes in GaAs, including ^{71}Ga, ^{69}Ga, and ^{75}As. Their nonzero spins are depicted by tiny gray arrows. The shaded areas show the wavefunction of the donor bound electron with thick black arrows representing their spins. The red wiggly arrow shows the incoming photon interacting with electrons. Note, that the electron wavefunction is smeared over $\approx 10^5$ nuclei and not shown to scale.

In quantum mechanics, the quantized angular momentum $\mathbf{L}$ based on the spin dimensionless operator $\mathbf{I}$ is defined as $\mathbf{L} = \hbar\mathbf{I}$ and acts as vector operator on the nucleus' spin state. Here, the total angular momentum operator, $\mathbf{I}^2$, and the projection in the direction of the z quantization ($\mathbf{I}_z$) can be measured simultaneously. In general,

$$\mathbf{I}^2 \left|\psi\right\rangle = \hbar^2 I(I+1) \left|\psi\right\rangle, \tag{2.1}$$
$$\mathbf{I}_z \left|\psi\right\rangle = m_z \hbar \left|\psi\right\rangle; \quad m_z = -I, ..., I.$$

As the size of the nucleus is much smaller than the lattice constant and the de-Broglie wavelength of the electrons, the nucleus can be considered as point-like with a magnetic dipole moment $\boldsymbol{\mu}$ associated to the spin angular momentum as $\boldsymbol{\mu} = \gamma_n \hbar\mathbf{I}$. Here, $\gamma_n = \frac{eg_n}{2m_p} = \frac{g_n\mu_N}{\hbar}$ is the nuclear gyromagnetic ratio given in Tab. 2.1 for all of the isotopes of GaAs. The nuclear magneton $\mu_N = \frac{e\hbar}{2m_p} = 5.05 \times 10^{-27}$ J/T is much smaller than the electron magnetic moment $\mu_B = 9.3 \times 10^{-24}$ J/T due to the large mass of nuclei[1] [48]. Consequently, even in relatively high magnetic field, the polarization of nuclei is typically negligible and polarization takes place via HFI with electrons. At the same time, only the nuclear spin system is isolated from the lattice making it a good candidate for recording information for long times. The energy of the nuclear spin system in an external magnetic field is small but relevant for spin dephasing and consists of two parts. One part is related to the spin-spin interaction including DDI and QPI for small fields and the second one is the Zeeman energy in case of high fields. Both are explained in detail in the following sections.

2.2.1. Dipole-Dipole Interaction

The magnetic-type nuclear spin interactions between neighboring nuclear magnetic moments are characterized by the DDI. Considering two neighboring nuclei, Fig. 2.3 (a), the energy interaction

---
[1] $\frac{m_e}{m_p} = 5.05 \times 10^{-4}$

Physical quantity	^{69}Ga	^{71}Ga	^{75}As
spin quantum number I	3/2	3/2	3/2
natural abundance %	60.108	39.892	100
$\frac{\gamma_n \hbar}{\mu_B} \, (\times 10^{-3})$	0.732	0.930	0.523
magnetic moment (μ_I/μ_N)	2.01659	2.562266	1.439475
quadrupole moment Q (barn)	0.171	0.107	0.314
hyperfine constant A_{HF} $(\mu\mathrm{eV})$	38	49	46
nuclear field b_N (T)	-1.37	-1.17	-2.76
electronic density $\eta \, (\times 10^3)$	2.7	2.7	4.5

Table 2.1.: Summary of the main physical quantities and their values for the isotopes of GaAs including two gallium isotopes ^{69}Ga and ^{71}Ga and the arsenic isotope ^{75}As [34, 49, 50].

from spin 2 with magnetic moment $\boldsymbol{\mu_2} = \gamma_2 \hbar \mathbf{I}_2$ on spin 1 with $\boldsymbol{\mu_1} = \gamma_1 \hbar \mathbf{I}_1$ apart from each other with distance[2] $\mathbf{r}_{12}$ is described by the Hamiltonian:

$$
\begin{aligned}
\mathcal{H}_{\mathrm{DDI}} &= -\boldsymbol{\mu_2} \cdot \mathbf{H}_{12} \quad\quad\quad\quad\quad\quad (2.2) \\
&= -\frac{\mu_0}{4\pi r_{12}^3} \boldsymbol{\mu_2} \cdot \left[\frac{3}{r_{12}^2} \mathbf{r}_{12} (\boldsymbol{\mu_1} \cdot \mathbf{r}_{12}) - \boldsymbol{\mu_1} \right] \\
&= -\boldsymbol{\mu_1} \cdot \mathbf{H}_{21},
\end{aligned}
$$

where μ_0 is the vacuum permeability and $\mathbf{H}_{12}$ ($\mathbf{H}_{21}$) is the magnetic field from spin 2 (1) experienced by spin 1 (2), respectively. This interaction depends on the distance of the two spins $\mathbf{r}_{12}$, the magnitude of the magnetic moments, and their orientation to $\mathbf{r}_{12}$ [51].

2.2.2. Local Field and Spin Temperature Concept

The field that each nucleus experiences from its adjacent nuclei is denoted as the local field (B_L). The spin precession of each spin in

---

[2]The distance is in this system large enough such that both dipoles can be described as point dipoles.
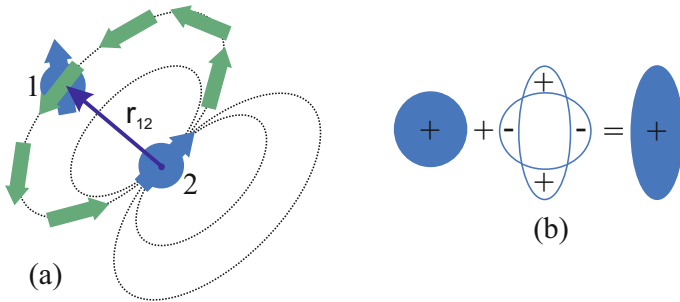
Figure 2.3.: Semi-classical picture of the spin-spin interaction. (a) A magnetic field produced by nuclear spin 2 affects nuclear spin 1. This is shown as hypothetical black curves with green arrows on top that show the direction of the field. The distance r_{12} is a vector joining the centers of the two spins. (b) A spherically symmetric positive charge together with a region of positive and negative charge on different poles results in a nonspherical prolate nucleus where a quadrupole moment exits [52].

this field results in the time T_2 which defines the transversal dephasing time within the nuclear spin system. This field differs from one semiconductor system to another but is usually on the order of a few mT. The corresponding dephasing time in semiconductors like GaAs is on the order of $(0.1 - 1 \text{ ms})$ [31], which is much faster than the longitudinal relaxation time T_1 in the presence of an external magnetic field. The dephasing time T_2 in a structure with a lattice constant a can be calculated by:

$$T_2 = \frac{1}{\gamma_n B_L} = \frac{\hbar a^3}{\mu_I^2}, \tag{2.3}$$

where $\hbar$ is the reduced Plank constant. In case of no effective magnetic field $B = 0$, the average nuclear spin is zero. On the other hand, when $B \neq 0$, the average nuclear spin follows:
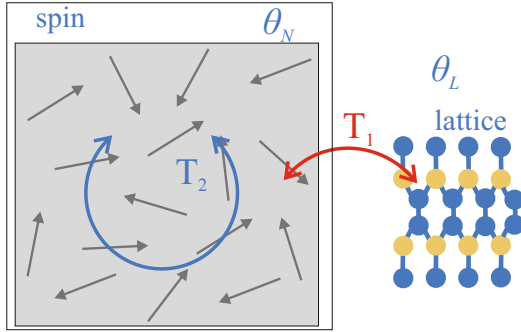
Figure 2.4.: In a system of nuclear spins (gray arrows) isolated from the lattice, a quasi equilibrium state characterized by spin temperature θ_N is reached within the transversal dephasing time T_2. Here, the lattice temperature is denoted with θ_L. The longitudinal relaxation time is T_1.

$$\langle I \rangle = \frac{I(I+1)}{3} \frac{\mu_I B}{k_B \theta_N}. \tag{2.4}$$

During the time T_2, a thermal equilibrium is established between the nuclei, which is characterized by a parameter known as spin temperature, θ_N [31,53–55]. This temperature can be different from the lattice temperature θ_L. Figure 2.4 illustrates the spin and the lattice temperatures schematically.

In case of $B \neq 0$, the ratio of population of the spin states separated by energy ΔE with spin temperature θ_N is given by the Boltzmann factor:

$$\frac{N_{\mathbf{I}_z}}{N_{\mathbf{I}_z-1}} = \exp(\frac{\Delta E}{k_B \theta_N}), \tag{2.5}$$

where $N_{\mathbf{I}_z}$ and $N_{\mathbf{I}_z-1}$ are the population of nuclear spin state $\mathbf{I}_z$ and $\mathbf{I}_z-1$, respectively. The spin temperature can be positive or negative depending on the relative direction of the nuclear polarization and
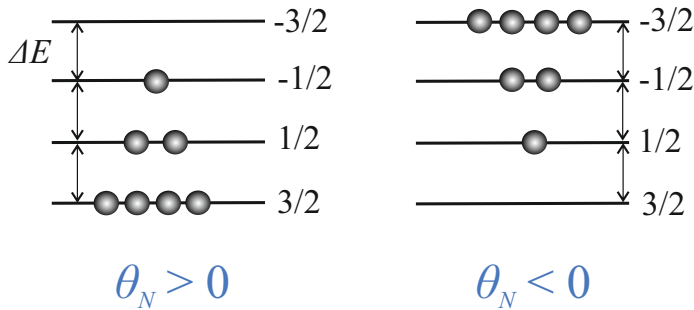
Figure 2.5.: Schematic illustration of the nuclear spin temperature for the positive (left) and negative (right) case. The energy states of a nucleus with $I = 3/2$ in an external magnetic field are shown as black horizontal lines. The splitting between the close energy states is shown with $\Delta E = g_n \mu_N B$, where g_n is the nuclear spin g-factor.

the external magnetic field. When the temperature is positive, the probability of finding an occupied spin state at a higher level is low. However, when the temperature is negative, higher energy states are more likely to be occupied. A negative spin temperature is "hotter" than a positive spin temperature. When a negative-temperature system comes in contact with a system with a positive temperature, energy is transferred to the positive temperature system according to the laws of thermodynamics. Figure 2.5 illustrates positive and negative nuclear spin temperature schematically.

2.2.3. Quadrupole Interaction

Nuclei can be considered as composite particles, and therefore the electric quadrupole moment and the QPI is nonzero for $I > \frac{1}{2}$ [56]. In this case, the charge distribution within a nucleus is not spherical any more and a nuclear quadrupole moment is present as illustrated in Fig. 2.3 (b).

The Hamiltonian responsible for the electronic quadrupole effect

$\mathcal{H}_{\text{QP}}$ can be derived via the Wigner-Eckart theorem [48, 50, 51, 57]. Considering the electric field gradient tensor at the nucleus as $V_{\alpha\beta}$ and the nuclear quadrupole operator $Q_{\alpha\beta}$ as

$$\mathcal{H}_{\text{QP}} = \Sigma_{\alpha\beta} V_{\alpha\beta} Q_{\alpha\beta}, \qquad (2.6)$$

$$V_{\alpha\beta} = e\Sigma_j \frac{\partial^2}{\partial r_{j\alpha} \partial r_{j\beta}} \left(\frac{1}{r_j} \right),$$

$$Q_{\alpha\beta} = \frac{eQ}{6I(2I-1)} \left[\frac{3}{2} (\hat{I}_\alpha \hat{I}_\beta + \hat{I}_\beta \hat{I}_\alpha) - \delta_{\alpha\beta} I^2 \right],$$

$$\Rightarrow \mathcal{H}_{QP} = \Sigma_{\alpha\beta} \frac{\partial^2 V}{\partial r_\alpha \partial r_\beta} \frac{eQ}{6I(2I-1)} \left[\frac{3}{2} (\hat{I}_\alpha \hat{I}_\beta + \hat{I}_\beta \hat{I}_\alpha) - I(I+1) \right],$$

where α and β are three axis directions (x, y, z) and e is the electron charge. The magnitude of the quadrupole moment Q for GaAs isotopes are listed in Tab. 2.1. Interestingly, coupling to phonons due to QPI affects the nuclear spin relaxation rate at finite temperatures which is explained extensively in section 4.10.1.

2.2.4. Zeeman Effect

The magnetic moment of the electrons[3] ($\mathbf{M} = g_e \mu_B \mathbf{S}$) in solid-state systems is coupled to the applied external magnetic field $\mathbf{B}$. This is known as the Zeeman interaction. The Zeeman energy of the electron spin in $\mathbf{B}$ is given by [48]:

$$\mathcal{H}_z = -\mathbf{M} \cdot \mathbf{B} = g_e \mu_B \mathbf{S} \cdot \mathbf{B}, \qquad (2.7)$$

where μ_B is the Bohr magneton and g_e is the electron g-factor. The splitting of the levels in the presence of an external magnetic field is shown in Fig. 2.6.

The Zeeman energy of a nuclear spin in the presence of $\mathbf{B} = B_0 \hat{z}$ is analogous [50]:

$$\mathcal{H}_z = -\boldsymbol{\mu} \cdot \mathbf{B} = -\gamma_n \hbar B_0 \mathbf{I}_z = -\mu_N g_n B_0 \mathbf{I}_z. \qquad (2.8)$$

---

[3] $\mathbf{S} = (\sigma_x, \sigma_y, \sigma_z)$ where $\sigma_{x,y,z}$ are the Pauli spin matrices.
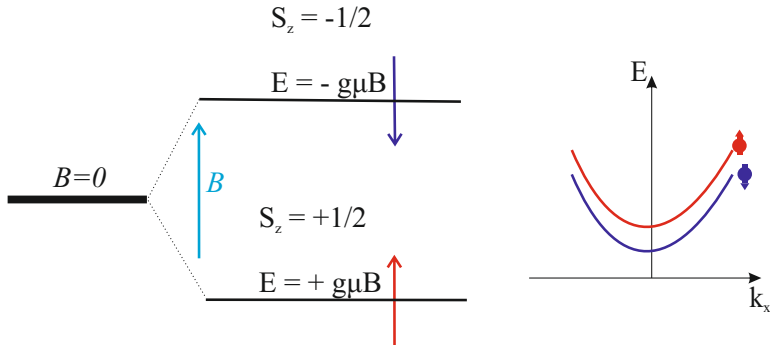
Figure 2.6.: (left) In the absence of a magnetic field, $B = 0$, the conduction band energy levels are degenerate. By applying a magnetic field, the optical spectral lines are splitted due to the two different spin orientations. The orientation of the spins of each energy state is illustrated by blue and red arrows. (right) The Zeeman effect results in the splitting of the energy E dispersion in the momentum (k)-space.

Nuclear Zeeman splitting is usually negligible, such that only the electron Zeeman splitting plays a crucial role in the spin flip-flop process from HFI [52].

2.3. Hyperfine Coupling of Electron-Nuclear Spin System

The electron spin $\mathbf{S}$ is connected to the nuclear spin $\mathbf{I}$ via the magnetic interaction known as HFI and plays a key role in the combined electron-nuclear spin system [31]. The Hamiltonian that describes this interaction is:

$$\mathcal{H}_{\mathrm{HFI}} = \frac{\mu_0}{4\pi}\gamma_e\gamma_n\hbar^2 \left[\frac{8\pi}{3}\delta(\mathbf{r_I})(\mathbf{I}\cdot\mathbf{S}) + \frac{3(\mathbf{I}\cdot\mathbf{r})(\mathbf{S}\cdot\mathbf{r})}{r^5} - \frac{\mathbf{I}\cdot\mathbf{S}}{r^3} \right]. \tag{2.9}$$

Here, μ_0 is the vacuum permeability, and γ_e and γ_n are the electron[4] and nuclear gyromagnetic ratios, respectively. Furthermore, $\delta(\mathbf{r_I}) = |\psi(0)|^2$ is the electron probability density at the position of the nucleus. For s-type orbitals, like conduction band electrons bound to shallow donors, the first term of Eq. 2.9 yields the strongest interaction. The dipolar interaction between electron and nucleus is described by the two other terms.

Considering just the first term and taking the average of the orbital coordinates, one can rewrite Eq. 2.9:

$$\mathcal{H}_{\mathrm{HFI}} = A_{\mathrm{HF}} \left[I_z S_z + \frac{1}{2}(I_+S_- + I_-S_+) \right]. \tag{2.10}$$

The hyperfine coupling constants, $A_{\mathrm{HF}} = \frac{\mu_0}{4\pi}\frac{8\pi}{3}\gamma_e\gamma_n\hbar^2|\psi(0)|^2$ have a value of around $100\,\mu\mathrm{eV}$ for GaAs, and are summarized in Tab. 2.1 for the three stable GaAs isotopes. The nuclear and electron spin raising and lowering operators are written as $I_\pm = I_x \pm iI_y$ and $S_\pm = S_x \pm iS_y$ where x, y, z are the three axis directions. Interestingly, the large value of A_{HF} in GaAs compared to other semiconductors like Si shows the considerable importance of HFI in GaAs. Generally, the effects from HFI can be divided into two groups: static and dynamic effects, which are addressed in the following.

2.3.1. Static Effect: Knight Field & Overhauser Field

In general, the static part of HFI related to the first term of Eq. 2.10 is connected to the fields experienced by electrons and nuclei due to their polarization. The magnetic field from polarized electrons on nuclei, KF, was first observed in 1949 by Knight as a shift of the

---

[4]$\gamma_e = \frac{g_0\mu_B}{\hbar}$; the free electron g-factor is $g_0 = 2.0023$.

expected NMR frequency in metals [28]. If the electrons are free, this field is weak, otherwise, the magnetic field felt by a nucleus from localized electrons in a lattice with unit cell volume v_0 is [48]:

$$B_e = -\frac{16\pi}{3}\mu_0 n_e \eta^2 = b_e \mathbf{S},\qquad(2.11)$$

where n_e is the electron concentration and η is the electronic density at the nucleus[5]. This field changes when an electron comes (goes) to (from) the localization center.

An electron localized at a shallow donor interacts with almost 10^5 nuclei within its Bohr radius a_B. Consequently, the net internal field from the polarized nuclei B_N (Overhauser field) changes the Zeeman energy of the electrons. This field (as the result of HFI over all nuclei) is proportional to the nuclear polarization [31]:

$$B_N = \Sigma_{\alpha=1}^3 \frac{16\pi N}{3g_e}\mu_{N,\alpha}\eta^2 \langle I_\alpha \rangle,\qquad(2.12)$$
$$= \Sigma_\alpha b_{N,\alpha}\frac{\langle I_\alpha \rangle}{I}.$$

Here, the sum is taken over all three isotopes, $\langle I_\alpha \rangle$ is the mean spin of the nuclei, and N is the number of nuclei. Each species of nuclei has a field[6] b_N and its sign is defined by g_e which is negative in GaAs. The related values for b_N and η of different GaAs isotopes are listed in Tab. 2.1. If in GaAs all nuclei are polarized, the total average nuclear field amounts to several Tesla [34].

2.3.2. Dynamic Nuclear Polarization

Based on the second term in Eq. 2.10, including raising and lowering operators, there is a flip-flop interaction between the electron and the nuclear spin system. In this process, the total spin and the total energy are both conserved and leads to phenomena like DNP

---

[5]In the case of homogeneity, $\eta = 1$.
[6]$b_N = 0.1$ mT for homogeneous electronic densities.

and NSR. This happens when the system is out of thermodynamic equilibrium. In this situation, electrons with higher energy do a flip-flop transition and transfer their energy to nuclei within their neighborhood. Therefore, DNP is the process of transferring angular momentum from electrons to nuclei via HFI resulting from any deviation in the electron spin system. This process was first proposed by Overhauser [33] and was the first method to measure the change of nuclear frequency due to the nonequilibrium electrons. Later, DNP as a result of photoelectrons was observed by Lampel [14] for ^{29}Si.

3. Experimental Procedure

In this work, the Hanle method is used to measure both electron and nuclear spin relaxation times. In section 3.1 of this chapter, the structure of the GaAs samples used in the experiments of this thesis is explained. In section 3.2, a summary of the Hanle method including the experimental setup and the procedure for measuring the ESR rate is provided. Section 3.3 is devoted to the oblique Hanle technique where the effect of the nuclear spin polarization on the electron spin polarization is also considered. The details of the setup and the procedure of the experiments to measure the NSR rate are explained as well.

3.1. Samples

All measurements are performed on specially designed GaAs samples with varying doping concentrations grown by molecular beam epitaxy. The thickness of the relevant GaAs epilayer is about 2 μm enclosed by specially adapted n-doped top and bottom capping layers in order to reduce the surface and interface effects from the depletion zone at the edge of the sample. In App. A, a detailed description of the sample structure is provided. In these samples, Si donors located at the position of Ga lattice sites are the most abundant impurities yielding n-doped GaAs. The doping regime covers the whole regime from strongly localized carriers up to the fully degenerate case. The nominal doping densities ranging from $n_d = 1.2 \times 10^{15}$ cm^{-3} to $n_d = 1.03 \times 10^{17}$ cm^{-3} are summarized in Tab. 3.1. These doping density values are determined from electrical transport measurements from Ref. [27]. Detailed parameters from the transport measurement of the same samples are accurately

Sample	S1	S3	S4
$n_d\left(10^{16}\text{cm}^{-3}\right)$	0.120(3)	0.658(9)	0.895(6)
Sample	**S5**	**S6**	**S7**
$n_d\left(10^{16}\text{cm}^{-3}\right)$	1.732(7)	1.65(6)	4.02(9)
Sample	**S8**	**S9**	**S10**
$n_d\left(10^{16}\text{cm}^{-3}\right)$	6.02(8)	8.20(5)	10.31(5)

Table 3.1.: Experimentally determined doping densities $n_d\left(10^{16}\text{cm}^{-3}\right)$ for the investigated GaAs samples (see Ref. [27] for further details on the equally named samples and the respective parameters from the temperature dependent Hall measurements).

described in Refs. [10, 27]. Several of these parameters are used in this thesis to explain the results *quantitatively* (see chapter 4).

3.2. Hanle Effect

The depolarization of the PL in an external transverse magnetic field (B_{ext}) - known as the Hanle effect - was first described by Wilhelm Hanle in 1924 [20] in the fluorescence of gases and later was applied in optical orientation experiments of semiconductors by Parson [15]. Here, partially spin-polarized electrons in the conduction band and holes in the valence band are generated via the absorption of circularly polarized light based upon angular momentum conservation. In bulk materials, the holes typically lose their spin orientation quasi immediately [6]. As a consequence, the projection of the electron spin average onto the direction of the excitation light beam, S_z, is proportional to the measured circular PL, ρ.

A transverse magnetic field B_{ext} applies a torque to such a spin polarized system. The spin rotates around B_{ext} with the Larmor precession frequency $\omega_L = \frac{g_e\mu_B B_{\text{ext}}}{\hbar}$ [31, 58]. As a result of this precession, polarization of the time averaged PL decreases as B_{ext} increases. Additional information on the calculations of the Hanle signal is described in App. B.
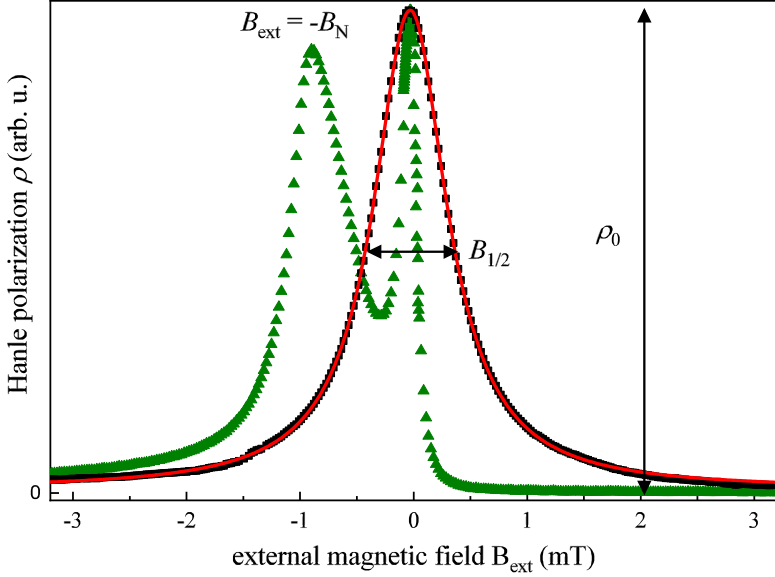
Figure 3.1.: The black squares depict a typical Hanle curve measured with 50 kHz modulation of the excitation polarization, i.e., without relevant optical pumping of the nuclear spin system, and the solid red line is the corresponding Lorentzian fit. The green triangles depict, in contrast, the measured Hanle curve for excitation with right circularly polarized light where dynamic nuclear spin pumping changes the shape of the Hanle curve drastically. Both Hanle curves are normalized to their respective maxima. The measurements are performed at 6.5 K for sample S7.

The black squares in Fig. 3.1 show a measured continuous-wave (CW) Hanle depolarization curve for sample S7. The spin's projection onto the observation direction clearly decreases as B_{ext} increases and can be described very accurately by the Lorentz curve:

$$\rho(B) = \frac{\rho_0}{1 + (\omega_L T_s)^2}.$$

(3.1)

Here, ρ_0 is the Hanle polarization signal at zero magnetic field. The solid red line in Fig. 3.1 shows a Lorentzian fit to the measured black squares according to Eq. 3.1. The electron spin lifetime T_s can be determined by the half-width at half maximum (HWHM) of the Lorentzian curve.

3.2.1. Relaxation Time Measured by the Hanle Effect

In general, the interaction of the magnetic moment μ with a magnetic field $\mathbf{B}$ applies a torque τ on the system and changes the angular momentum $\mathbf{L}$ of the system:

$$\tau = \frac{d\mathbf{L}}{dt} = \mathbf{M} \times \mathbf{B},$$

(3.2)

where the total magnetic moment of the sample is known as magnetization $\mathbf{M} = \gamma \mathbf{L}$ with $\gamma = \dfrac{g\mu_B}{\hbar}$ as the gyromagnetic ratio. The dynamics of the magnetization in a magnetic field was first calculated by Felix Bloch [59] in a set of equations called Bloch equations. Considering three components of the magnetization (M_x, M_y, M_z), the equilibrium magnetization $M_{z,0}$, and a longitudinal magnetic field B_z, Bloch equations in terms of individual components and relaxation terms are [6]:

$$\frac{dM_{x,y}}{dt} = \gamma(B_z M_{y,x}) - \frac{M_{x,y}}{T_2},$$

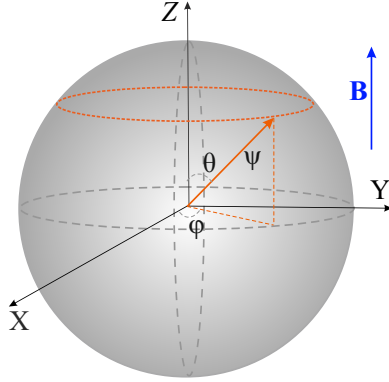$$\frac{dM_z}{dt} = \frac{M_z - M_{z,0}}{T_1}.$$

(3.3)

Figure 3.2.: A representation of the Bloch sphere with θ and φ as polar and azimuthal angles. Any pure state is defined as $|\psi\rangle = \cos\frac{\theta}{2}|\uparrow\rangle + e^{i\varphi}\sin\frac{\theta}{2}|\downarrow\rangle$ based on spin up $|\uparrow\rangle$ and down $|\downarrow\rangle$. The magnetic field is along the Z direction.

Here, two decay times T_2 and T_1 represent the spin-spin and the spin-lattice relaxations, respectively. As shown in Fig. 3.2, each electron spin at a specific state on the Bloch sphere has a transverse component in the XY plane specified by the angle φ and a longitudinal component with the angle θ. The transverse component rotates with the Larmor frequency ω_L around $\mathbf{B}$ while the longitudinal component is constant. The transverse decoherence time T_2 indicates how long individual spins are in phase. In other words, it is the time that the ensemble of electron spins loses the phase because of fluctuations of the frequencies. The longitudinal decay time T_1 is the spin-lattice relaxation time in solids during which an electron spin loses energy equal to the Zeeman energy $\Delta E = (\hbar\omega_L = \gamma_e\mu_B B_z)$ and relaxes to a ground state. Therefore, after this time, thermodynamic equilibrium is established between the lattice and the spin system. Indeed, it is also called thermal relaxation. Each factor that results in T_1 can also change the phase coherence and thus results in the limit $T_2 \leq 2T_1$ [60, 61]. In anisotropic environments, inho-

mogeneities affect the T_2 time. In these systems, the value and/or the direction of the magnetic field changes, and/or different electron g-factors g_e leads to different ω_L. Therefore, the Larmor precession frequency of each spin is different from the other. It implies an inhomogeneous spin dephasing time known as T_2^* which is often smaller than T_2.

An important factor affecting the spin dephasing time is the correlation time τ_c based on a model defined by Pines and Slichter [60]. During this time, the spin ensemble interacts with the environment causing a change $\delta\omega$ in the precession frequency and a phase change $\delta\phi = \delta\omega\tau_c$. Based on this model, the T_2 dephasing time equals the time of having $\langle\Delta\phi\rangle = 1$ after n interactions. In this case, $\frac{1}{T_2} = (\delta\omega)^2\tau_c$. When the magnetic field is small $\gamma B \ll \frac{1}{\tau_c}$, the Zeeman splitting is also small, and the spin dephasing in the surrounding environment is the same in all directions. Accordingly, measuring in either transversal or longitudinal direction does not make any difference, and thus $T_1 = T_2$.

The Hanle method measures the transverse spin dephasing time [6, 62, 63]. In the experiments presented in this thesis, the applied magnetic field is less than 20 mT resulting in a Larmor period which is almost 70 ns. The correlation time is much smaller $\tau_c \ll 1$ ns [10], such that $T_1 = T_2$ holds throughout and is rather denoted by τ_s. The inhomogeneity of the g-factors can in principle also play a role [64] but are too small to influence the Hanle measurements of this thesis significantly.

3.2.2. Hanle Setup

Figure 3.3 shows the experimental setup for the measurements in this work using the Hanle-type PL depolarization scheme. The excitation source is a CW laser with an oval-shaped output light mode which is corrected by an anamorphic prism pair. The wavelength of the laser is 785 nm corresponding to a photon energy of 1.58 eV. The excitation intensity is always kept so low that the fraction of the optically injected carriers remains at least a factor of a hundred below the doping density. In the experiments presented in this thesis,
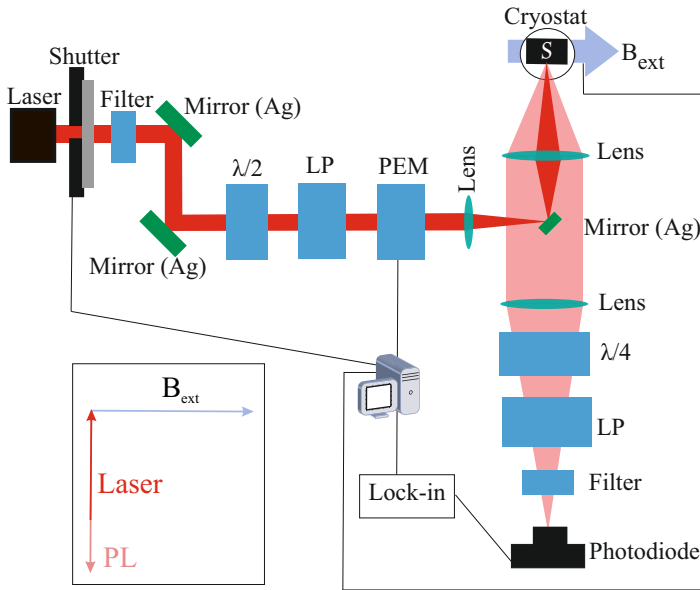
Figure 3.3.: Schematic representation of the experimental setup for measuring the ESR rates in n-type GaAs samples via a Hanle-type depolarization scheme. (inset): The propagation direction of the laser at the sample is perpendicular to the external magnetic field and parallel to the growth direction of the samples.

the light intensity is as low as 0.2 Wcm^{-2} at the sample surface. In this way, there is no significant disturbance of the electron ensemble from thermal equilibrium. Furthermore, the low energy states are unpolarized due to Pauli blocking, and no spin polarization is possible. Consequently, spectrally resolved PL measurements confirm in a control experiment [10] that this degree of circular polarization results from carrier recombination at the Fermi energy.

An 800 nm short pass filter ensures that no residual light emission from the laser diode compromises the PL detection. The intensity control of the optical excitation is performed by a rotatable half-wave plate ($\lambda/2$) in combination with a linear polarizer (LP). The LP also guaranties a very well defined linear polarization.

A 50 kHz photoelastic modulator (PEM), set to $\lambda/4$ retardance, alternates the linear polarization of the laser light between left (σ_+) and right (σ_-) circularly polarized light. The reason to choose 50 kHz goes back to frequency-dependent measurements of the DNP [10]. Nuclear polarization is negligible in these Hanle experiments for modulation frequencies above 2 kHz. Other publications confirm the observation e.g., Ref. [65]. In Fig. 3.1, the black squares correspond to the standard Hanle curve (no nuclear field). In this situation, the excitation was rapidly modulated between left (σ_+) and right (σ_-) circularly polarized light, which efficiently suppresses the build-up of nuclear spin polarization. The green triangles represent the depolarization of the electron spins in the oblique Hanle measurement where a strong B_N is induced.

For the experiments performed in this thesis, the samples are placed in a microcryostat, which can be cooled down to 4 K. Two pairs of magnetic coils are placed around the cryostat. The first pair shields in Helmholz configuration the earth's magnetic field at the sample position, along the direction of the PL detection. The second pair consists of electromagnets creating a magnetic field B_{ext} perpendicular to the direction of the excitation light. The inset of Fig. 3.3 illustrates the relative orientation of B_{ext}, excitation light, and PL. The degree of circular polarization of the emitted PL is detected in reflection geometry by a Si photodetector and a lock-in amplifier. In this path, the PL is transmitted through a $\lambda/4$, a LP

and a high-quality longpass filter and focused on the photodetector with a lens. The longpass filter is used to efficiently block laser reflections.

3.2.3. Experimental Procedure to Measure the ESR Rate
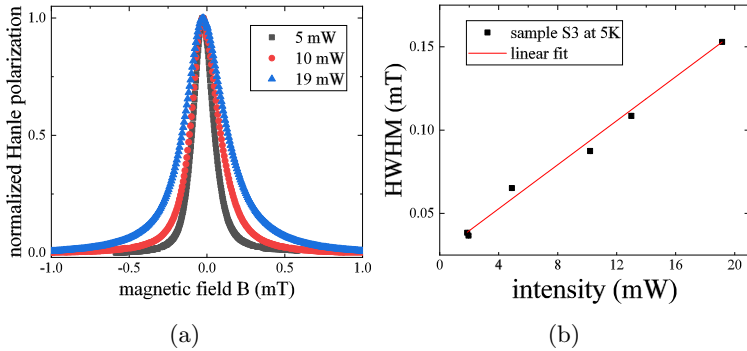

(a)   (b)

Figure 3.4.: (a) Hanle depolarization measurements for different laser intensities for sample S3 at 5K. (b) Linear dependence of the HWHM of the Hanle curve on intensity.

The HWHM of the Lorentzian shaped Hanle curve is the most important parameter derived from a Lorentz fit to the experimental data. Based on Eq. 3.1, the HWHM is a direct measure of the effective ESR rate $\frac{1}{T_S}$ which is the sum over the recombination rate[1] $\frac{1}{\tau_r}$ and the spin relaxation rate $\frac{1}{\tau_S}$ [66]:

$$\frac{1}{T_S} = \frac{1}{\tau_S} + \frac{1}{\tau_r}. \tag{3.4}$$

If the condition $\tau_s \ll \tau_r$ is met, τ_S and T_S are in good approximation equal. This is possible when the laser intensity approaches

---

[1]τ_r equals the electron lifetime.

zero. To this end, the width of the Hanle curve is measured at different intensities and the data is extrapolated to zero with a linear fit. The intercept of the fit is used to determine the ESR rate for each sample. Figure 3.4 (a) and (b) illustrate an example of the procedure to measure τ_S. The width of the Hanle curve has in good approximation the expected linear dependence on intensity.

3.3. Oblique Hanle

The optical pumping of electrons by circularly polarized light induces a macroscopic nuclear magnetic field ($B_N \neq 0$) according to the DNP effect which strongly modifies the effective magnetic field and thereby the shape of the Hanle curve [31]. The effective nuclear magnetic field influences the electron spin orientation in the same way as an external magnetic field, and the footprint of this nuclear magnetic field is directly imprinted on the ESR rate. In other words, the nuclear magnetic field impacts the electron spin dynamics by either enhancing or weakening the external magnetic field's effect, i.e., the electron spin rotates around the total effective magnetic field $B_\mathrm{ext} + B_N$,

$$\Omega = (g_e \mu_B / \hbar) \left(B_\mathrm{ext} + B_N \right). \qquad (3.5)$$

In the situation where the angle between the exciting light and the magnetic field differs from 90°, measuring of the nuclear field via the Hanle effect becomes easily possible. This Hanle effect in the oblique field is named as "oblique Hanle" in this thesis. In Fig. 3.5, the respective angle α is schematically illustrated together with the relative orientation of the laser, external magnetic field, and PL. The nuclear polarization is in general in the direction of the electron spin polarization. Selecting a small angle α ($\approx 10°$ deviation from the Voigt axis) gives rise to both transverse and longitudinal components of the nuclear spins in respect to B_ext whereat the longitudinal component of the nuclear field is directed either parallel or antiparallel to the external field. This longitudinal component impacts the depolarization of the electrons in the oblique Hanle
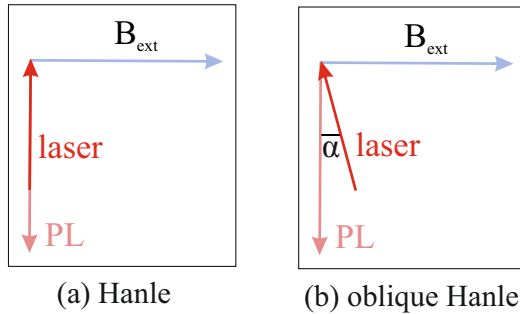
(a) Hanle (b) oblique Hanle

Figure 3.5.: Orientation of the laser, the external magnetic field, and the PL relative to each other: (a) In the standard Hanle technique, B_{ext} is perpendicular to the excitation laser light. (b) In the oblique Hanle technique, a small angle α between the excitation laser and the magnetic field gives rise to a significant nuclear spin polarization.

experiment [67]. The transverse component precesses around B_{ext} such that the time-averaged transverse component is zero in the case of CW excitation, i.e., the transverse nuclear spin component does not play a role in this experiment.

Figure 3.1 illustrates the result of the oblique Hanle setup as green triangles together with the result of the standard Hanle setup as black squares. Both are measured by slowly sweeping the amplitude of the external magnetic field and measuring at the same time the degree of PL polarization.

3.3.1. Changes to Hanle Setup to Measure the NSR Rate

In order to measure the nuclear spin's effect, some changes are applied to the Hanle setup in Fig. 3.3.

- The positions of the PEM and the $\lambda/4$ plate are exchanged. In this way, the polarization of the laser light is kept fixed, and an efficient build-up of nuclear spin polarization is possible.

- The sample inside the cryostat is rotated by about $10°$ in order to enable both nuclear spin polarization and the detection of the nuclear polarization via the Hanle effect in a nearly Voigt geometry setup.

- A computer controlled shutter switches the laser excitation after DNP off, in order to study the evaluation of the nuclear spin dynamics while no electrons and holes are excited.

In this situation, the detection path includes: a 50 kHz PEM, a linear polarizer, an 800 nm longpass filter, a photodiode, and a lock-in amplifier.

3.3.2. Experimental Procedure to Measure the NSR Rate

The NSR rate is measured following a well-established three-stage temporal scheme: (I) optical nuclear spin initialization, (II) nuclear spin relaxation in the dark, i.e., without optical excitation, and (III) measurement of the remaining nuclear spin polarization by a Hanle-like polarization measurement of the PL. Figure 3.6 schematically depicts the respective measurement protocol. This protocol has been first proposed and realized by Kalevich *et al.* [68], and is an indirect method based on the cooling of the nuclear spin system.

After the dynamic polarization of the nuclear spins by 300 s of optical pumping, the laser excitation is switched off by an electrically controlled mechanical shutter for a variable dark time t_{dark}. During this dark time, the optically induced nuclear spin polarization, which is directly related to an effective nuclear magnetic field B_N, decays towards its equilibrium state.

The technique utilizes the shift of the Hanle curve due to nuclear spin polarization. For each sample, two preparatory Hanle and oblique Hanle measurements were carried out as the first step to identify the optimal magnetic field B_{pump} for the detection of the nuclear spin polarization (see Fig. 3.1). These measurements are necessary in order to choose an external magnetic field for the actual
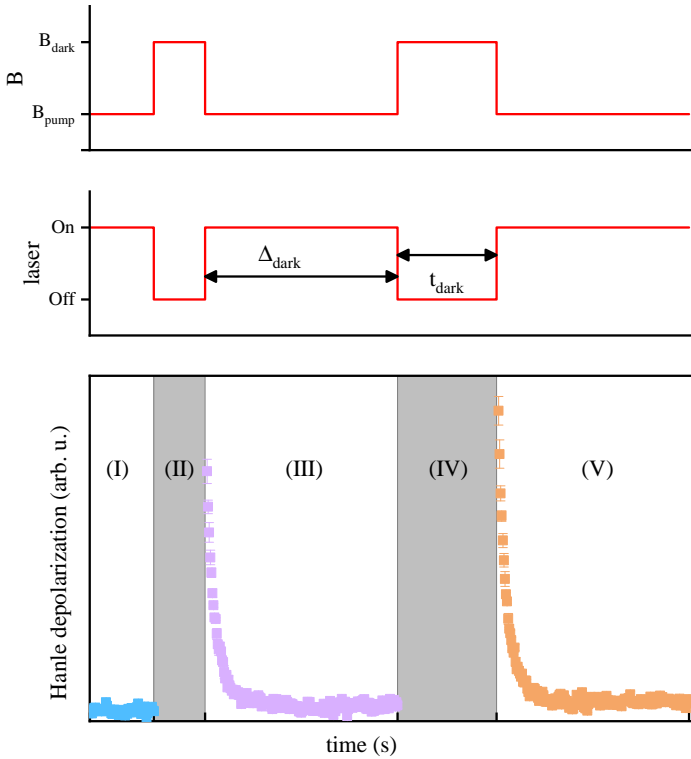
Figure 3.6.: Illustration of the Hanle depolarization protocol (I): Initial dynamic polarization of the nuclei with laser light. (II): The laser is switched off (dark time) and the nuclei relax in the dark. (III) Repolarization stage where the laser is switched on again and the temporal change of the Hanle signal is measured while the nuclei are dynamically polarized again. The procedure is repeated with longer dark times and the fixed bright time (shown with (IV) and (V)). During the laser light-on stage, the external magnetic field is set to B_{pump}, and when the laser is off, B_{dark} is applied. The magnetic field B_{pump} is set to a point where the electron spins are the most sensitive to the nuclear Overhauser field. The height of Hanle depolarization of each bright section defines ρ_{dark}.

measurement (B_{pump}) where the change of the PL polarization by change of B_N is largest and yields an optimal signal to noise ratio. After t_{dark}, the shutter is opened again and the external magnetic field is switched to B_{pump}. Here, the degree of circular polarization of the PL is measured time-resolved in reflection geometry. In principle, the degree of circular polarization directly after opening the shutter, ρ_{dark}, is already a good measure of B_N after t_{dark}. However, measuring the temporal change of the PL polarization during optical excitation and extrapolating this transient to the time where the shutter is opened increases the measurement accuracy of ρ_{dark}, and accordingly, of the effective B_N. In practice, the nearly Voigt geometry allows combining the optical pumping of the nuclear spin ensemble and the measurement of the remaining nuclear spin polarization from the previous pump process into one step.

All of the measurement procedures explained above are used to investigate the B_N in the samples listed in Tab. 3.1. The measurement results are explained extensively in part II of chapter 4.

4. Experimental Results

In this thesis, the electron and nuclear spin relaxation rates in a set of n-GaAs samples are investigated employing the Hanle and oblique Hanle techniques, respectively. The experimental results of this thesis are distinguished into two parts within the following chapter. In part I, the experimental results of the temperature dependence of the ESR rate for three samples (S3, S6, and S10) is presented. A *quantitative* calculation of the mechanisms, including a short discussion of the underlying spin relaxation mechanisms, is presented in this part as well. Part II is devoted to the NSR results in dependence of magnetic field (section 4.8), doping (section 4.9), and temperature (section 4.10). The relevant mechanisms involved in the NSR dynamics include the Korringa mechanism, spin diffusion, and the effect of phonons.

Part I.

Results for the Electron Spin Relaxation Rate

4.1. Electron Spin Relaxation

In the field of spintronics the quest for the longest spin relaxation time in GaAs stands representative for the desire of a complete quantitative understanding of the ESR [22, 24, 25, 69–73]. In 1997, Kikkawa *et al.* reported the longest up to then measured ESR time (100 ns) in a bulk n-GaAs sample with a doping concentration of $n_d = 10^{16}$ cm^{-3} [22]. Later, an even longer relaxation time (300 ns) for n-GaAs samples was reported [74]. Dzhioev *et al.* provided a detailed study of a set of n-GaAs in order to explain the relevant ESR mechanisms. Their doping dependence result showed that different mechanisms are involved below and above the MIT [25].

Recently, Lonnemann *et al.* [27] gave a more comprehensive picture of the doping dependence of the ESR at a fixed temperature of 6.5 K in a contiguous set of bulk n-GaAs samples, combining optically detected spin dynamics with magneto-transport measurements. The way the spin interacts with its environment depends primarily on its spatial dynamics, which in turn can be directly extracted from the experimental magneto-transport measurements from Ref. [27]. The acquired information on the spatial correlation time affects the impact of local hyperfine fields and momentum-dependent magnetic fields. The correlation time is an important parameter that depends on the type of interaction. For localized carriers, the VRH mechanism, and for free carriers, the momentum scattering time determines the value of this correlation time. These transport experiments pave the way for *quantitatively* explaining the mechanisms involved in spin relaxation. Below the MIT, as the doping rises, the decrease of the HFI and the increase of the VRH leads to an increase of the relaxation time with a maximum relaxation time of 800 ns just below the MIT. The DP mechanism resulting from the motional narrowing regime is valid at and above the MIT.

This particular non-monotonical dependence of the ESR rate on doping at a fixed temperature was the main motivation to investigate the corresponding temperature dependence of the ESR rate in three specially selected n-GaAs samples studied in Ref. [27]. The

first sample has a doping density of just below the MIT (sample S3 with the doping $n_d = 6.58(9) \times 10^{15}$ cm^{-3}). This sample showed the longest ESR time in Ref. [27] indicating a transition point from HFI and VRH mechanisms to the DP mechanism. The second sample (sample S6 with the doping $n_d = 1.65(6) \times 10^{16}$ cm^{-3}) has a doping density directly at the MIT where Ref. [27] has shown a strong change of the momentum scattering angle. The third sample (sample S10 with the doping $n_d = 1.031(5) \times 10^{17}$ cm^{-3}) has a doping density clearly above the MIT. Reference [27] has shown for this sample the dominance of the degenerate DP (deg-DP) mechanism at 6.5 K and temperature dependent measurement for this sample is expected to show a transition to the non-degenerate DP (nondeg-DP) mechanism.

4.2. Experimental Results

The measured temperature dependence of the ESR rate for sample S3 is shown as orange dots in Fig. 4.1. With increasing temperature, the ESR rate decreases between 4 K and 7 K and increases afterwards above 7 K. This non-monotonous behavior of the ESR rate with temperature reflects the impact of the different ESR mechanisms which are plotted in Fig. 4.1 as well. At low temperatures, the HFI between atomic nuclei and electrons dominates the spin relaxation. This mechanism is depicted as an orange dotted line in Fig. 4.1. With increasing temperature, the VRH mechanism accelerates the spin relaxation (shown as a green dotted line in Fig. 4.1). For the high-temperature range, the charge carriers are entirely delocalized into the conduction band, and the DP mechanism dominates the spin relaxation.

The fully numerical calculated DP contribution is shown as a red dotted line, whereas the Boltzmann approximation valid in the non-degenerate regime is shown as a purple dotted line, respectively. The sum over HFI, VRH, and deg-DP mechanisms is shown as a blue line, demonstrating a perfect coincidence with the measured data. The relative impact of these mechanisms is accounted for by
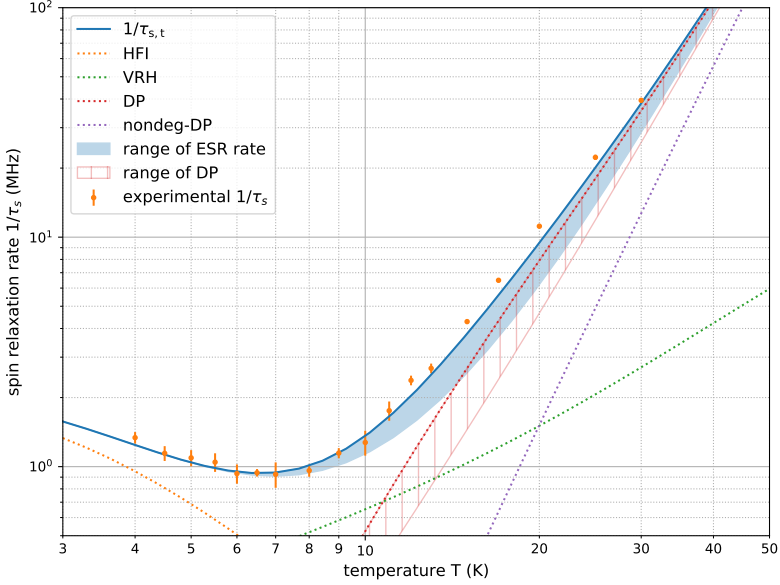
Figure 4.1.: Measured ESR rate for sample S3 as a function of temperature (orange dots with error bars). Here, the HFI and the VRH relaxation mechanisms are plotted as orange and green lines, respectively. The DP mechanism is depicted as a red dotted line assuming a temperature dependent scattering weight $\gamma_3(T)$. The purple dotted line shows the effect of nondeg-DP with $\gamma_3 = 6$. The sum over these three mechanisms as the total relaxation rate $(\tau_{s,\,t}^{-1})$ is plotted as a solid blue curve for the whole measured temperature range. The blue shaded and the red hashed areas indicate the uncertainty on the weighting arising from the imponderability of the exact conduction band carrier density at low temperatures and low dopings.

weighting with the respective occupancy of the affected states, i.e., localized and conduction band states. However, an uncertainty concerning the exact weighting for this low-doped sample remains, since the available transport data naturally bear a relatively high uncertainty on the exact conduction band carrier density at low temperatures. The blue shaded (and red hashed) area in Fig. 4.1 reflects this uncertainty by either using the density related to the conductivity (upper limit) or Hall density measurements (lower limit). Furthermore, the proportionality factor γ_3^{-1} connecting the momentum relaxation and the correlation time, is assumed to change with temperature and thus affects the ESR rate. The reasoning behind this assumption is equivalent to the findings on the doping dependence of γ_3 between the MIT and the degenerate limit. At low temperatures (low doping) the spatial dynamics of the carriers in the conduction band is strongly affected by the local potential corrugations arising from the donor distribution, thus leading to a large angle scattering behavoir which corresponds to $\gamma_3 = 1$. In the other extreme of high temperatures (high doping) this effect is diminished leading to the *classical* value of $\gamma_3 = 6$ for small angle scattering [31]. The range in-between is interpolated using the same weighting as for the relative impact of the spin relaxation mechanisms. The complete calculation is explained in detail in Sec. 4.3.

Figure 4.2 illustrates the ESR rate for the sample at the MIT (S6) in dependence on temperature. For this sample, the ESR rate increases steadily with increasing temperature in the whole measured range. For such doping densities (directly above the MIT) and low temperatures, the conductivity is a mixture of metallic and hopping contributions. Therefore, in principle all three mechanisms (HFI, VRH, and deg-DP) could contribute to the ESR with the relevant weighting factors. However, the HFI mechanism has a negligible contribution ($\ll 1$ MHz) to the ESR process and is thus not shown in Fig. 4.2. The result for the sum over the three mechanisms is plotted in Fig. 4.2 as a solid blue line. At high temperatures, the nondeg-DP mechanism is also plotted as a purple dotted line.

The ESR rate for sample S10, depicted in Fig. 4.3, is nearly constant at low temperatures. In the density regime above the second
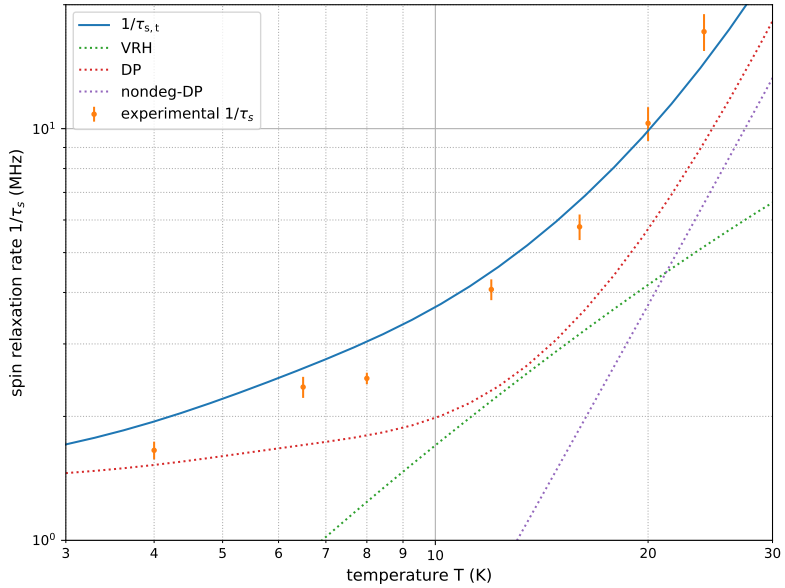
54

Figure 4.2.: Orange points with error bars show the measured ESR rate for sample S6. The effect of the VRH is plotted as a green dotted line. For this sample, deg- and nondeg-DP are plotted with red and purple dotted lines, respectively. The total ESR rate for the whole measured temperature is plotted as a solid blue line.
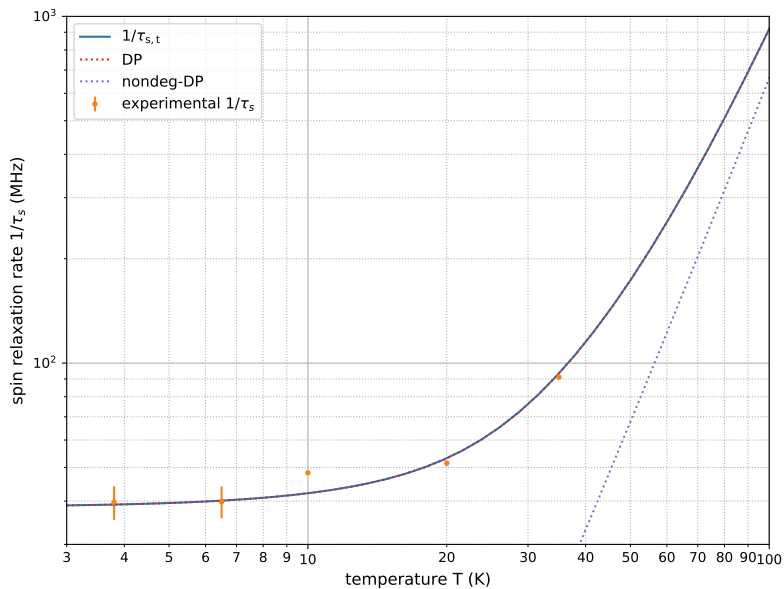
Figure 4.3.: The orange points with error bars are the measured relaxation rate for sample S10. The calculated total relaxation rate is plotted as blue line and equals in extremely good approximation the calculated DP relaxation rate (shown as red dotted line) over the whole range of temperature. For high-temperatures, the nondeg-DP is plotted as a purple line.

critical transition - which applies to this sample S10 - the Fermi energy lies fully in the conduction band. Thus, the primary mechanism in this sample is the DP mechanism (the red dotted line) which is at such high electron densities much more efficient compared a) to the contributions of the other mechanisms and b) to the other two samples due to the higher spin dependent splitting at the Fermi level. For higher temperatures, the ESR rate increases and gradually approaches the non-degenerate limit shown as a purple dotted line in Fig. 4.3.

In the following, we will present a quantitative model which is an extension of the model presented in Ref. [27] and describes the temperature and density dependence of Γ_s with very high accuracy especially in the regime of the MIT. The model combines all relevant spin relaxation mechanisms and takes as input parameters temperature dependent magneto-transport data measured on the same samples. These electrical transport data are detrimental for a quantitative calculation of Γ_s since they provide for example the doping densities and the localization potentials within an unpretentious transport model (see Table 4.1 for a list of the extracted transport parameters for S3, S6, and S10). Reference [27] presents the relevant transport data for a set of ten high quality n-GaAs samples such that the whole carrier density regime from strongly localized over the MIT up to significant conduction band filling is covered. Interpolation of these parameters allows extraction of the relevant parameters for any high quality n-GaAs:Si sample and finally a realistic, quantitative calculation of Γ_s for any reasonable doping concentration and any temperature below room temperature. Oertel *et al.* [70] present ESR measurements in GaAs at and above room temperature where a significant number of electrons in the high energy tail of the Fermi distribution are not within the limit of motional narrowing.

The following theoretical description is based on the three relevant ESR mechanisms HFI, VRH, and DP at which the impact of HFI and VRH are weighted by the degree of electrons localized in the impurity band, W_{di}, and the contribution of DP is weighted by the

Table 4.1.: Experimentally determined doping densities n_d^{exp}, and the relevant parameters from transport measurements for the three investigated n-GaAs samples.

Sample No.	S3	S6	S10
$n_d{}^{\text{exp}}$ $\left(1 \times 10^{16}\text{cm}^{-3}\right)$	0.658(9)	1.65 (6)	10.31 (5)
AE_{loc} (eV)	0.0001	0.00105	0.00245
n_{loc} $\left(10^{15}\ \text{m}^{-3}\right)$	5.86263	3.45401	-
E_{E} (meV)	1.84	1.0	-
N_{EF} $\left(10^{25}\ \text{m}^{-3}\right)$	2.27268	8.7576	-
σ_m $(1/\Omega\text{cm})$	0.0	1.29	44.0
A_{II}^0 $\left(10^{23}\ (\text{mVs})^{-1}\right)$	1.24	1.26	1.33
μ_{P}^0 $\left(\text{m}^2(\text{Vs})^{-1}\right)$	0.68	0.505	0.32
T_0 $\left(10^2 K\right)$	89.7	23.3	-
σ_0 $(1/\Omega\text{cm})$	7.25	14.2	-

degree of free electrons in the conduction band, W_{cb}.

$$
W_{di} = \frac{n_{\text{di}}(T)}{n_{\text{di}}(T) + n_m(T)},
$$
$$
W_{cb} = 1 - W_{di}.
$$

(4.1)

Here, $n_{\text{di}}(T)$ and $n_m(T)$ are the temperature dependent densities of the impurity band electrons and free electrons in the conduction band, respectively. Note, that for the lowest doped sample no impurity band exists and the free carrier density is directly calculated by thermal activation into the conduction band with the corresponding activation energy E_E taken from the temperature dependent conductivity measurements. For samples S6 and S10 the respective densities are obtained from temperature dependent Hall density measurements within the two band model (see [27] for details). Note, that for S10 there exists effectively only carriers in the conduction band.

4.3. Dyakonov-Perel Mechanism

In atoms and solids, the spin-orbit interaction (SOI) couples the spin of the carriers to the spatial movement. Indeed, this inevitable coupling can be the result of structural inversion[1] asymmetry (Rashba) or bulk inversion asymmetry (Dresselhaus). This SOI can be seen as an effective magnetic field in which the spins precesses. The direction (and the amount) of this effective magnetic field depends on the momentum of the electrons **k**. Spin relaxation of electrons in this effective magnetic field is described by the DP spin relaxation mechanism [6, 48, 50, 75–79]. The foundation of DP is explained in App. D in more details.

For conduction band electrons with momentum k and energy E_k, the DP spin relaxation rate follows [6, 31, 70, 78, 80]

$$\tau_{\text{s, DP}}^{-1}(E_k) = \frac{32}{105} \alpha^2 \frac{\tau_p}{\gamma_3} \frac{E_k^3}{\hbar^2 E_g}.$$ (4.2)

Here, E_g is the energy gap[2] and α is a dimensionless parameter based on the Dresselhaus constant $\gamma_D = 19.0(5)$ eVÅ^3 and defines the strength of the SOI

$$\alpha = \frac{\gamma_D}{\hbar^3} \sqrt{8 m_e^* E_g}.$$ (4.3)

The ratio between correlation time τ_c and momentum scattering time τ_p is described by a factor $\gamma_3 = \frac{\tau_p}{\tau_c}$. The value of γ_3 depends on both doping and temperature. If either of these two factors increases, more delocalized electrons can be found in the conduction band. Therefore, since γ_3 increases the momentum scattering of free electrons in the conduction band results from small-angle Rutherford scattering. However, near the MIT the momentum scattering is isotropic due to the local conductivity from random-positioned

---

[1] In inversion symmetry each point at (x, y, z) to the inversion symmetry center has a corresponding point at (-x, -y, -z).
[2] E_g=1.59 for $T = 0$ K

donors occurs. The doping dependence of γ_3 from S6 to S10 follows at 6.5 K a linear dependence[3,4]

$$\gamma_3(n_d) = 6.67 \times 10^{-17} \text{ cm}^{-3}(n_d - n_{c1}) + 1, \qquad (4.4)$$

and changes from $\gamma_3 = 1$ for the MIT sample to $\gamma_3 = 6$ for S10 [27]. The temperature dependence of γ_3 for S3, S6, and S10 is accordingly modeled by:

$$\gamma_3(T) = \begin{cases} \gamma_3(n_d) + (\zeta - 1) \times (6 - \gamma_3(n_d)), & \text{for S6 and S10;} \\ \gamma_3(n_d) + W_{cb} \times (6 - \gamma_3(n_d)), & \text{for S3.} \end{cases}$$
$$(4.5)$$

4.3.1. Numerical calculating the DP Mechanism

In order to obtain a thermal average of the DP spin relaxation rate, Eq. 4.2 has to be averaged over all available energies with the corresponding density of states and level occupation:

$$\tau_{s, \text{ DP}}^{-1} = \frac{\int_0^\infty \tau_{s,\text{DP}}^{-1}(E_k)\, f_{\text{FD}}(E_k)\, [1 - f_{\text{FD}}(E_k)]\, \rho(E_k)\, dE_k}{\int_0^\infty f_{\text{FD}}(E_k)\, [1 - f_{\text{FD}}(E_k)]\, \rho(E_k)\, dE_k}, \quad (4.6)$$

where the Fermi-Dirac distribution f_{FD} is [81]

$$f_{\text{FD}}(E_k) = \left(1 + \exp(\frac{E_k - E_F}{k_B T})\right)^{-1}. \qquad (4.7)$$

In Eq. 4.6, the quasi-equilibrium spin polarization is approximated by $f_{\text{FD}}(E_k)\, [1 - f_{\text{FD}}(E_k)]$ for small spin polarization, i.e., a small difference between the Fermi energies of spin up and spin down electrons. The density of states $\rho(E_k)$ starting from the conduction band in a volume of V is

---

[3]For more information of the doping dependence of γ_3, please see Ref. [27].
[4]Here, $n_{c1} = 1.6 \times 10^{16}$ cm^{-3} is the first critical density marking the MIT transition.

$$\rho(E_k) = \frac{V}{2\pi^2}\left(\frac{2m_e^*}{\hbar^2}\right)^{\frac{3}{2}}\sqrt{E_k}. \qquad (4.8)$$

In order to define the momentum scattering time τ_p in Eq. 4.2, the Hall conductivity from the transport measurement is calculated as follows [27]

$$\tau_p = \frac{\sigma\, m_e^*}{1.04e^2 n_\mathrm{m}}, \qquad (4.9)$$

with the conductivity

$$\sigma = \sigma_\mathrm{cb}\left(T\right) + \sigma_\mathrm{m,0} + \sigma_\mathrm{VRH}\left(T\right). \qquad (4.10)$$

The conductivity is assumed to be a sum of two contributions: conduction band conductivity σ_cb and a conductivity of delocalized carriers in the impurity band via VRH (σ_VRH)(see Sec. 4.4). If the doping is high enough, a metallic conductivity $\sigma_\mathrm{m,0}$ contributes as well. The two-channel conductivity in the conduction band is

$$\sigma_{cb}(T) = \frac{e\, n_d}{\frac{1}{\mu_{II}(T)} + \frac{1}{\mu_{PO}(T)}}\, \exp(-\frac{E_E}{k_B T}). \qquad (4.11)$$

The mobility due to scattering on ionized impurities μ_{II} and scattering on polar optical phonons μ_PO are

$$\mu_{II}\left(T\right) = \frac{A_{II}^\mathrm{RT}}{n_d}\left(\frac{T}{300K}\right)^{3/2}, \qquad (4.12)$$

$$\mu_\mathrm{PO}\left(T\right) = \mu_{PO}^\mathrm{RT}\left(\frac{T}{300K}\right)^{-2.3}, \qquad (4.13)$$

where μ_{PO}^RT and $\frac{A_{II}^\mathrm{RT}}{n_d}$ are mobilities at room temperature. A summary of the conductivity measurement and more details on the formulas are provided in App. C.

4.3.2. Non-degenerate DP Mechanism

At sufficiently high temperatures, the system is non-degenerate and the electron spins follow the non-degenerate DP mechanism. In this case, the thermal averaging of Eq. 4.2 is over the Boltzmann distribution $\langle f_{\mathrm{MB}}(E_k)\rangle = \frac{2}{\sqrt{\pi}}(k_B T)^{-3/2}\exp(-\frac{E_k}{k_B T})E_k^{1/2}$ [6,31] and follows

$$\tau_{s,\text{nondeg-DP}}^{-1} = Q\frac{\alpha^2\left(k_B T\right)^3 \overline{\tau}_p}{\hbar^2 E_g}, \qquad (4.14)$$

where

$$\overline{\tau}_p = \langle\tau_p(E_k)E_k\rangle/\langle E_k\rangle \qquad (4.15)$$

is the average momentum relaxation time and

$$Q = \frac{16}{35}\gamma_3^{-1}\frac{\langle\tau_p E_k^3\rangle}{\langle\tau_p E_k\rangle} \qquad (4.16)$$

is a scaling factor which depends on the effective scattering process. For ionized impurity scattering with $\tau_p \propto E_k^{3/2}$ one obtains $Q = \frac{64}{7}\times\gamma_3^{-1}$ where $\gamma_3 = 1$ is the limit for large and $\gamma_3 = 6$ for small angle scattering.

4.3.3. Limiting Cases of the DP Mechanism

In the limit of non-degeneracy at high temperature, Eq. 4.6 can be approximated by the averaging over the Maxwell-Boltzmann distribution f_{MB} instead of Fermi-Dirac distribution f_{FD}. However, the difficulty lies in calculating the transition between the low and the high temperature regime with only $\overline{\tau}_p$ being available from transport measurements. At low temperatures $\overline{\tau}_p(E)$ approaches $\tau_p(E)$ since a Fermi distribution in Eq. 4.15 acts like a Dirac delta function at low temperatures at the Fermi energy.

In order to elucidate this problem analytically all constants are set to unity and the extreme cases for the high temperature is considered. The average momentum scattering time can be calculated in two ways:

1. $\bar{\tau}_p = \frac{\int_0^\infty E_k \, \tau_p(E_k) \, f_B(E_k) \, dE_k}{\int_0^\infty E_k \, f_B(E_k) \, dE_k} = 128\sqrt{2\pi}T^{3/2}$.

2. $\tilde{\tau}_p = \frac{\int_0^\infty \tau_p(E_k) \, f_B(E_k) dE_k}{\int_0^\infty f_B(E_k) \, dE_k} = 64\sqrt{2\pi}T^{3/2}$.

Using τ_p by either of these two cases makes a difference of two for the relaxation rate. For the first case, the Conwell-Weisskopf formula [82] is used to give the energy dependence of the momentum relaxation time

$$\frac{1}{\tau_p(E_k)} = \frac{n_{\text{ii}}Z^2 e^4}{16\sqrt{2\pi}\epsilon^2 \, (m_e^*)^{1/2}} E_k^{-3/2} \ln\left(1 + \frac{16\pi^2\epsilon^2 E_k^2}{Z^2 e^4 n_{\text{ii}}^{2/3}}\right). \quad (4.17)$$

where $\epsilon = \epsilon_r\epsilon_0$ is the dielectric constant and n_{ii} is the ionized impurity doping at energy E_k and $Z = 1$. However, for the second case, the experimentally extracted τ_p is used.

The factor ζ

The Fermi-Boltzmann factor ζ is approximated by the ratio of carriers obeying the Fermi-Dirac Boltzmann statistics plus unity.

$$\zeta = 1 + \frac{n_d}{N_{\text{eff}}(T)\exp(\frac{E_F - E_c}{k_B T})}. \quad (4.18)$$

Here, E_F and E_c are Fermi and conduction band energies[5], respectively. This weighting factor ζ is used in order to bring the numerical calculation in accordance with the analytical one regarding the excess of the average momentum relaxation time. Please note that ζ is set to two for S3 throughout.

4.4. Variable Range Hopping

The corresponding formula for the ESR rate via VRH between two donors with distance R_{ij} is:

---

[5]In the calculation of this thesis, $E_c = 0$.

$$\tau_{s,\,\text{VRH}}^{-1} = \frac{2}{3} \left\langle \theta^2(R_{ij}) \right\rangle / \tau_{\text{hop}}. \tag{4.19}$$

Here, $\theta(R_{ij})$ is the rotation angle that an electron spin undergoes during each hop. This angle derived by Gorkov and Krotkov [83] is

$$\theta(R_{ij}) = \frac{2\gamma_D}{\hbar^3} \sqrt{\frac{8}{35} (m_e^{*3} E_{\text{d}})} \frac{R_{\text{opt}}}{a_B}, \tag{4.20}$$

where $E_{\text{d}} = 5.8$ meV and $a_B = 10$ nm are binding energy and the Bohr radius, respectively. Moreover, $\gamma_D = 19$ eVÅ^3 is the Dresselhaus constant. The transport hopping time from transport measurement equals the correlation time τ_c in the case of hopping:

$$\tau_c = \frac{(R_{\text{opt}})^2}{6 D_{\text{hop}}}, \tag{4.21}$$

where $R_{\text{opt}} = \left[9 a_B / (8\pi N_{E_F} k_B T)\right]^{1/4}$ is the optimal hopping distance and the density of states at the Fermi energy E_F is N_{E_F}. To calculate the specific diffusion constant

$$D_{\text{hop}} = \frac{\sigma_{\text{hop}}(T) k_B T}{e n_{\text{H}}}, \tag{4.22}$$

the temperature dependent conductivity $\sigma_{\text{hop}}(T)$ resulting from the hopping process is used

$$\sigma_{\text{hop}}(T) = \sigma_0(N_{E_F}) T^{-1/2} e^{-[T_0(N_{E_F})/T]^{1/4}}, \tag{4.23}$$

where

$$T_0(N_{E_F}) = 512 / \left(9\pi k_B a_B^3 N_{E_F}\right), \tag{4.24}$$
$$\sigma_0(N_{E_F}) = \nu_H e^2 N_{E_F} R_{\text{opt}}^2 / 6,$$

with the phonon frequency $\nu_H = 8.8$ THz. More information about this mechanism is provided in App. E. The doping density n_{H} participating in hopping is

$$n_{\mathrm{H}} = n_{\mathrm{di}} - n_{\mathrm{cb}} \qquad (4.25)$$

where n_{di} is the delocalized carrier density from the impurity states. In App. C, the process of the Hall measurements is explained.

4.5. Hyperfine Mechanism

Below the MIT, the number of donors is low, the distance between donors is large, and the donor-bound electrons are considered localized. Each localized electron feels the effect of almost 10^5 atomic nuclei within its Bohr radius a_B. Here HFI is effective and can be expressed by the effective nuclear magnetic field, B_N [26]. Therefore, in the case of localized electrons, their spin precession around B_N is independent of each other, and the interaction between electrons can be ignored. The impurity and the conduction band do not overlap.

This also results in a phase angle: $\delta\phi = \pm\delta\omega\tau_c$ [60]. In case of a short correlation time, $\delta\omega\tau_c \ll 1$, motional-averaging formula should be used for the time of ESR rate in B_N:

$$\tau_{s,\,\mathrm{HFI}}^{-1} = (\frac{\mu_B g^*}{\hbar})^2 B_N^2 \tau_c \qquad (4.26)$$

where the $g^* = (0.484 - 6.3\,\mathrm{eV}^{-1}E)$ is the energy dependent effective electron g-factor [84, 85].

Part II.

Results for the Nuclear Spin Relaxation Rate

4.6. Nuclear Spin Relaxation

The coupling of the nuclear magnetic moments and the lattice determines to a large extend the relaxation dynamics of solid-state nuclear spins. This section presents the measurements of the NSR rate in a set of n-GaAs samples. The measurements are performed by using the three-stage experimental procedure explained in chapter 3. The dependence of NSR on doping and temperature for magnetic fields higher than the local field as two main external factors affecting the NSR are included in this section. The experimental results are explained with the involved theoretical mechanisms. Parts of the results are published in Ref. [86].

4.7. Nuclear Magnetic Field

The NSR rate is measured by repetitive application of the measurement protocol explained in section 3.3, i.e., (I) optical nuclear spin initialization, (II) nuclear spin relaxation in the dark, and (III) measured of the remaining nuclear spin polarization in dependence on the dark time t_{dark}.

Figure 4.4 illustrates exemplarily the respective change of the Hanle depolarization measured for different t_{dark} for sample S8. The amplitude of the Hanle polarization signal at $t = 0$ s, ρ_{dark}, is a measure of the remaining nuclear polarization which clearly depends on t_{dark}. In fact, ρ_{dark} increases with increasing t_{dark} since the nuclear spin polarization decreases. On the other hand, the transient Hanle polarization decays exponentially during the PL measurement due to the re-pumping of the nuclear spin polarization to its initialization value. Each Hanle transient is measured for 300 s for all of the measurements. In Fig. 4.4, just a few numbers of t_{dark} are plotted to have a better overview of the procedure.

The precise amplitude at $t = 0$ s, ρ_{dark}, is extracted by an exponential fit to these transients and used to calculate the remaining nuclear magnetic fields after t_{dark} by [31]
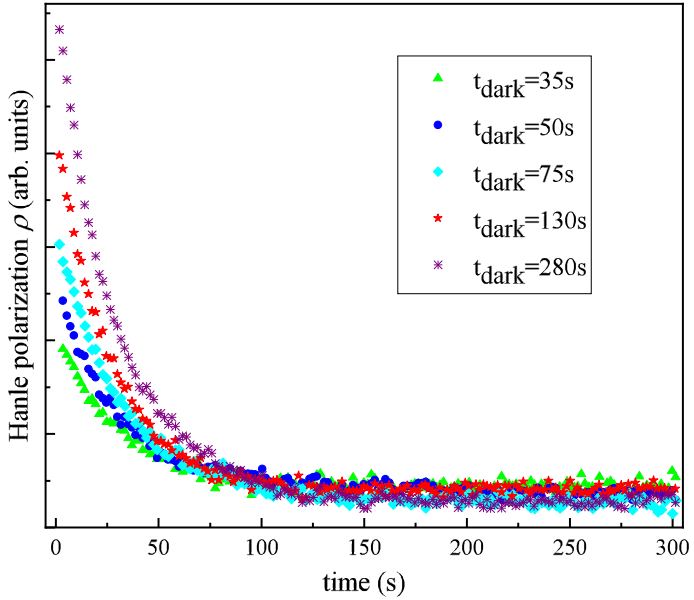
Figure 4.4.: Hanle depolarization transients recorded after different dark times for sample S8. In this example, the magnetic field during dark time is set to $B_{\mathrm{dark}} = 1.17$ mT. The measurement temperature is $T = 6.5$ K.

$$B_N = B_{1/2}\sqrt{\frac{\rho_0 - \rho_{\text{dark}}}{\rho_{\text{dark}}}} - B_{\text{pump}}. \qquad (4.27)$$

The corresponding value for B_N is plotted in Fig. 4.5. This figure shows exemplarily the measured B_N in dependence on t_{dark} for sample S5 with $n_d = 1.73 \times 10^{16}$ cm^{-3} and $B_{\text{dark}} = 2.344(44)$ mT. The resulting B_N can be well fitted by a single exponential decay which yields the NSR rate Γ. The solid blue line in Fig. 4.5 is an exponential fit which yields an NSR rate $\Gamma = 0.005\,50(21)$ Hz.
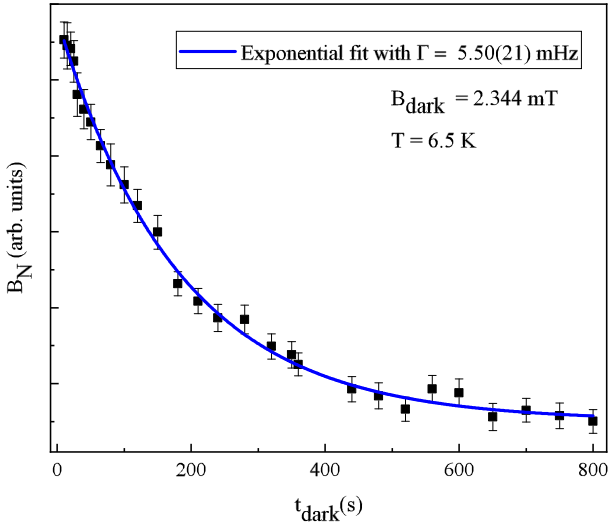
Figure 4.5.: The black squares are the measured nuclear magnetic field B_N in dependence on t_{dark} for sample S5 at one specific B_{dark} and T. The blue line depicts a single exponential fit yielding a NSR rate of $\Gamma = 0.005\,50(21)$ Hz.

4.8. Magnetic Field Dependence of the NSR Rate

The magnetic field dependence of the NSR rate can be derived via a density matrix formalism which is explained in Refs. [51,53,87,88] and yields

$$\Gamma(B_{\text{ext}}) = \Gamma_{\text{Z}} \frac{B_{\text{ext}}^2 + \xi\, B_L{}^2}{B_{\text{ext}}^2 + B_L{}^2}. \tag{4.28}$$

Here, $\xi = \Gamma_{\text{ss}}/\Gamma_{\text{Z}}$ is a fitting parameter, Γ_{ss} and Γ_Z are the spin relaxation rates originating from the spin-spin and the Zeeman interaction, respectively. In other words, ξ shows the relative impact of the local field B_L and the external field B_{ext}, respectively.
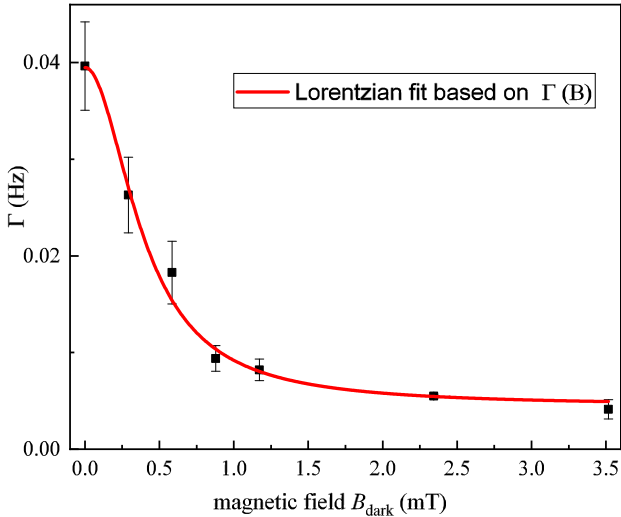
Figure 4.6.: Measured NSR rate Γ (black squares) as a function of B_{dark} at $T = 6.5$ K for sample S5 with $n_d = 1.73 \times 10^{16}$ cm^{-3}. The red solid line is a fit to the data according to Eq. 4.28 with $\xi = 8.79(74)$ and $B_L = 0.39(4)$ mT.

Sample	ξ
S1	16.21352 ± 10.28189
S3	16.21352 ± 10.28189
S4	7.10311 ± 1.38645
S5	8.79059 ± 0.7449
S7	7.43216 ± 0.41099
S8	10.56694 ± 2.78872
S9	6.38481 ± 0.41375
S10	11.62513 ± 2.85221

Table 4.2.: The values for ξ derived as a free parameter from the magnetic field dependence of Γ.

The magnetic field dependence of Γ for different B_{dark} is depicted in Fig. 4.6 as an example for sample S5 with $n_d = 1.73 \times 10^{16}$ cm^{-3}. The NSR rate follows the Lorentzian like function of Eq. 4.28.

The value for ξ in my measurements is a free parameter in the fit function in Fig. 4.6. These values are provided in Tab. 4.2 for all of our measured samples. Interestingly, these values are on average larger than the maximal theoretical estimated limit of 2 to 3 given in Ref. [53] for low magnetic fields which might be surprising at first. However, not only our measurements but also other measurements in the literature yield values much higher than 3 [44,87]. This could be attributed to additional relaxation mechanisms contributing to Γ_{ss} at zero external fields, as pointed out also in Ref. [89].

The local magnetic field is directly extracted from Eq. 4.28. The resulting B_L are depicted as blue squares with error bars in comparison to literature values in Fig. 4.7. This doping dependence of B_L shows on the whole a comparable increase with doping from 0.35 mT at $n_d = 1.2 \times 10^{15}$ cm^{-3} to 0.9 mT at $n_d = 1.03 \times 10^{17}$ cm^{-3} which lies well within previously determined values. Please note that the literature values are not measured on a contiguous set of samples like in this thesis but with different optical methods on different GaAs bulk and microstructure samples with varying strain leading to significant scattering of these values [90–92].
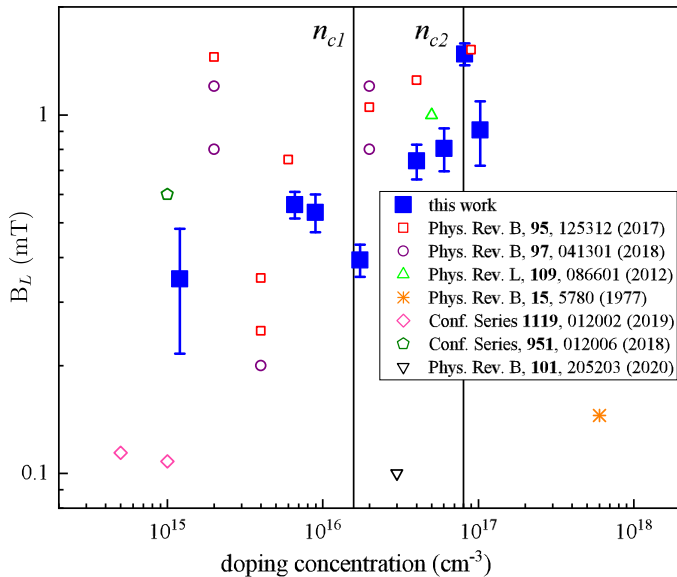
Figure 4.7.: Local field B_L in dependence on doping density. The measured values of our work are shown as blue squares, while the other symbols are from literature. The black vertical lines denote the so-called critical densities n_{c1} and n_{c2}.

4.9. Doping Dependence of the NSR Rate

Figure 4.8 shows the measured high field NSR rate Γ as orange dots with error bars in dependence on doping concentration for a lattice temperature of 6.5 K. The error bars of Γ are in turn extracted from exponential fits of B_N versus t_{dark} which is exemplarily shown for $n_d = 1.73 \times 10^{16}$ cm^{-3} in Fig. 4.6. The error bars of B_N are extracted from the exponential fits of the PL polarization versus laboratory time. The two vertical lines in Fig. 4.8 denote the critical densities $n_{\mathrm{c1}} = 1.6 \times 10^{16}$ cm^{-3} and $n_{\mathrm{c2}} = 8 \times 10^{16}$ cm^{-3}, i.e., the point of finite conductivity in the limit of zero temperature at the Mott MIT and the onset of impurity band hybridization with the conduction band, respectively. At low doping concentrations $n_d < n_{\mathrm{c1}}$, Γ increases monotonically with increasing n_d reaching a maximum around n_{c1}. For $n_d > n_{\mathrm{c1}}$, Γ decreases in turn with increasing n_d and becomes in good approximation independent of n_d around n_{c2}.

As figure 4.8 depicts, two relaxation mechanisms explain the behavior of the doping dependence of Γ. These are plotted as green dashed line (diffusion related NSR Γ_D) and as blue dashed-dotted line (Korringa NSR Γ_K). Both mechanisms are explained in detail in the following two chapters. The total NSR rate $\Gamma = \Gamma_D + \Gamma_K$ is shown as a red solid line. For $n_d < n_{c1}$, nuclear spin diffusion to localized electrons acting as nuclear spin killing centers results in relaxation of the nuclear spin polarization. As the doping increases, the number of localized electrons increases and subsequently the NSR rate due to spin diffusion rises. For $n_d > n_{c1}$, not only the relative but even the total number of fully localized donor electrons starts to decrease with increasing n_d. As a consequence, Γ_D decreases and becomes negligible for doping densities above the n_{c2}. At the same time, the number of delocalized electrons increases with increasing doping concentration, and consequently, the NSR rate increases according to the Korringa mechanism.
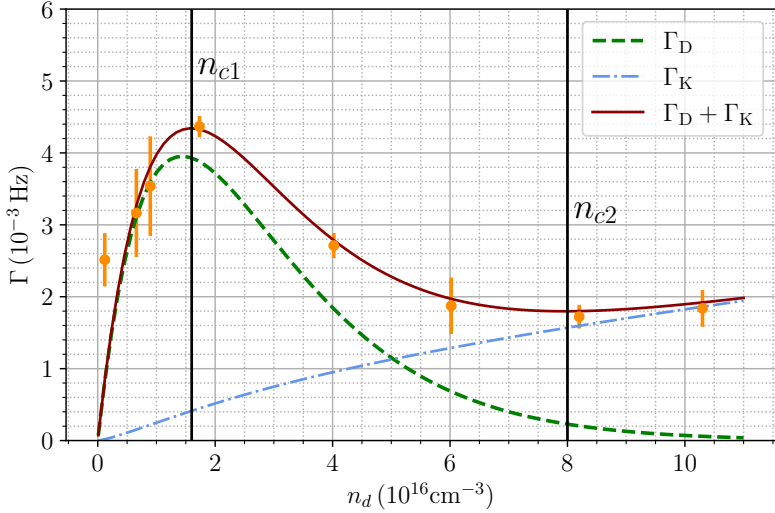
Figure 4.8.: Measured doping dependence of the high field NSR rate Γ in n-type bulk GaAs at $T = 6.5$ K (orange dots). The NSR rate due to diffusion to localized electrons Γ_D, is shown as green dashed line. The fully delocalized fraction of n_d enters the Korringa rate Γ_K according to Eq. 4.35, which is shown as blue dashed-dotted line. The values n_{c1} and n_{c2} denote the critical densities.

4.9.1. Spin Diffusion Effect

NSR in n-doped GaAs is strongly influenced by the presence of donor electrons [31, 36, 37, 42, 48, 50, 87, 93–95]. Localized donor electrons interact at low temperatures very efficiently via hyperfine contact interaction with the nuclear spin system. The resulting NSR times are only fractions of a second for nuclei, which are located within the Bohr radius a_B of a localized donor electron [46]. The spin relaxation of remote nuclei is at finite external magnetic fields typically orders of magnitude slower since the spin diffusion towards these relaxation centers is rather slow. In Fig. 4.9, the

diffusion process is illustrated schematically.
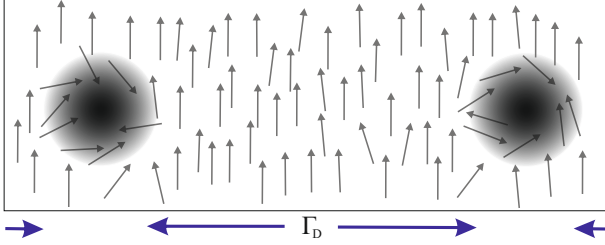
Figure 4.9.: A schematic illustration of the nuclear spin diffusion. The grey arrows represent the nuclear spins. The shaded black areas show the wavefunction of the donor-bound electrons. The warm-up of all other nuclei is via spin diffusion towards the donor sites, which is shown with the arrows below.

The NSR rate due to diffusion, Γ_D, can be approximated for low donor densities, n_d, and zero temperature by [96]:

$$\Gamma_D \approx 4\pi D_{\mathrm{av}} n_d a_B. \qquad (4.29)$$

Here, D_{av} is an average nuclear spin diffusion coefficient for the three isotopes of GaAs. Equation 4.29 describes the typical bulk NSR rate Γ only for n_d well below the MIT, $n_d^{-1/3} \gg a_B$, and for temperatures where ionization of the localized donor electrons can be neglected. However, the density of localized donors acting as effective drains for the nuclear spin polarization differs significantly for conditions deviating from these constraints. The relative number of fully localized donor electrons decreases with increasing n_d due to the increasing overlap of the donor wavefunctions. As a consequence, the at first linear increase of Γ_D with increasing n_d in Eq. 4.29 becomes sub-linear.

In order to calculate Γ_D quantitatively, the total number of donors n_d in Eq. 4.29 is replaced by the number of localized electrons $n_{\mathrm{d,\,loc}} = \eta \cdot n_d$. The fraction of localized electrons η acting as efficient drains for the nuclear polarization is
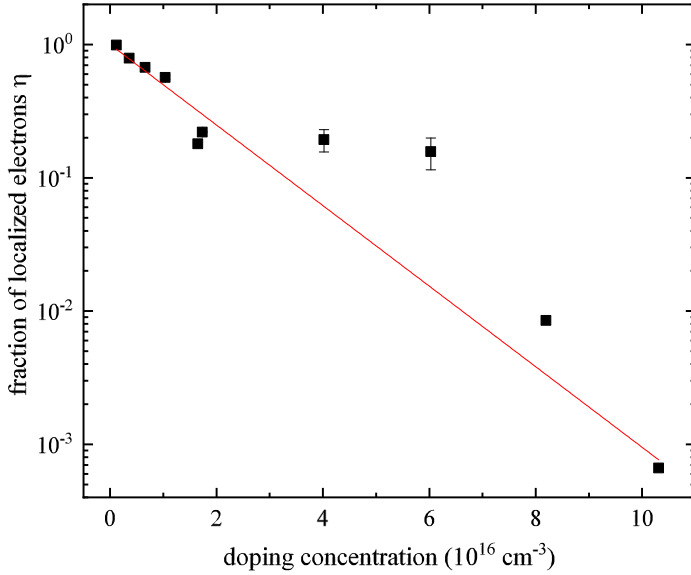
Figure 4.10.: Dependence of the localization fraction η on doping density. The red line shows a fit according to Eq. 4.31.

$$\eta = 1 - \frac{n_H^{6.5 \text{ K}}}{n_d}, \tag{4.30}$$

where $n_H^{6.5 \text{ K}}$ is the Hall carrier density at 6.5 K and n_d is the doping density extrapolated from the high temperature Hall measurements. The experimental transport data include already the ionization of the localized donors due to the finite temperature. A summary of these Hall measurements are provided in App. C of this thesis. The extracted η can be fitted by

$$\eta = e^{-n_d/\alpha_n}, \tag{4.31}$$

which is shown as red line in Fig. 4.10 for all of the measured samples. A finite deviation of η calculated from the measured $n_H^{6.5 \text{ K}}$

with Eq. 4.30 is not surprising for $n_d > n_{c1}$. Here, not only the localization of single donor electrons but also the localization of ensembles of donor electrons start to play a role. In contrast to single localized electrons, such localized ensembles of interacting electrons are not as efficient nuclear spin "killing centers". From the fit in Fig. 4.10, $\alpha_n = 1.43(20) \times 10^{16}$ cm^{-3}.

Such an exponential relation between the number of isolated single donors and n_d follows directly from Poisson statistics which also allows for a theoretical estimation of the constant α_n. With $\mu = n_d/n_\ell$, where n_ℓ is the lattice site density of the host crystal, the probability that a donor does not occupy a site is $e^{-\mu}$. The exclusive volume, where no other donor overlap exists is $V_{no} = \frac{4\pi}{3}(2 \cdot a_B)^3$. The probability $p(n_d)$ of finding a single donor which wavefunction - extending over its Bohr radius a_B - is non-overlapping with other donors, is given with $N_{no} = V_{no} \cdot n_\ell$ as

$$p(n_d) = \prod_{i=1}^{N_{no}} e^{-\mu} = e^{-\frac{32}{3}\pi a_B^3 n_d}. \qquad (4.32)$$

The prefactor in the exponent in Eq. 4.32 equals the experimentally determined α_n for an effective Bohr radius of $a_B^{\text{eff}} \approx 12.8$ nm which is only slightly larger than the typical donor Bohr radius for Si dopants in GaAs. Such a slightly larger radius is not unexpected since the donor electron wavefunction extends beyond a_B. Also, screening and any other interaction effects have not been considered in this basic estimate.

In Fig. 4.8, Γ_D (Eq. 4.29) is plotted as a green line where the number of localized electrons is used for the calculation. The only adjustable parameter for this fit is the average nuclear spin diffusion constant which lies with $D_{av} = 0.63 \pm 0.06 \times 10^{-13}$ cm^2/s in the same range as previously measured values [35, 36, 41].

The donor electron HFI is not a simple hard sphere drain center for nuclear spins. Furthermore, the values for D_{av} differ for the three different isotopes for $B \gg B_L$. Therefore, the result of this measurement is rather precise concerning Γ but not concerning a general value for D_{av}.

4.9.2. Korringa Mechanism

In metallic systems, where a free electron model can be assumed, HFI with the delocalized electrons is the dominant mechanism for the relaxation of nuclear spins. However, this relaxation by conduction electron spins is not just limited to metals, and also exists in semiconductors, like for the case of high doping densities above the MIT in n-GaAs. Instead of very efficient local relaxation centers, the nuclear spins interact at high doping densities with spin fluctuations of the electron gas. The NSR in the region of the MIT at finite temperatures is slightly more complex since the localization of the donor electrons changes with increasing n_d due to the overlap of the electron wavefunctions and the resulting coexistence of strongly localized electrons, weakly interacting donor electrons, the occurrence of impurity bands, and the occupancy of the conduction band.

A simultaneous electron spin-flip and nuclear spin-flop in the opposite direction is induced via this interaction. For this, an energy of $\hbar(\omega_e - \omega_n)$ is provided[6] by an equal change in the electron kinetic energy of only a fraction $(k_B T / E_F)$ of conduction electrons located around the Fermi energy E_F. Therefore, the average kinetic energy of the relevant electrons is of the same order of magnitude as the Fermi energy but much larger than the thermal energy $k_B T$. With the assumption of having one electron per atomic volume, the fluctuating local field of this electron affects nuclei during $\tau_c = \hbar / E_F$. In order to find out the transition probability of an electron from state E to E', a random perturbation $\hbar \mathcal{H}(t)$ with a short correlation time τ_c is considered [87],

$$\frac{1}{T_1} \sim |\overline{\mathcal{H}_{\mathrm{HFI}}^2}| \tau_c k_B T / E_F. \tag{4.33}$$

Here, the HFI Hamiltonian $\mathcal{H}_{\mathrm{HFI}}$ is given by Eq. 2.9. A weighting factor of $f(E)(1 - f(E'))$ shows the simultaneous probability of having an initial occupied state E and a final empty state E'. Here,

---

[6] Here, ω_e and ω_n are the electron and nuclear Larmor frequencies, respectively.

f is the Fermi distribution function based on Eq. 4.7. If the transition involves a simultaneous electron-nuclear spin flip, the change in kinetic energy between two energy states is small $E = E'$, and in the neighbourhood of Fermi energy $f(E)(1 - f(E'))$ is replaced by

$$f(E)(1 - f(E')) \sim k_B T. \tag{4.34}$$

Considering also the density of states at Fermi energy $\rho(E_F)$, and integrating over all of the energies, the total probability is described via the Korringa mechanism [38, 39, 42, 87, 97] by

$$\Gamma_K = \frac{\pi}{\hbar} A_{\text{HF}}{}^2 v_0^2 \rho^2(E_F) k_B T, \tag{4.35}$$

where A_{HF} is the hyperfine constant from Eq. 2.10. As is clear from Eq. 4.35, the Korringa mechanism does not depend on the magnetic field. The salient feature of this relaxation is the linear dependence of the relaxation rate with temperature. Γ_K is plotted in Fig. 4.8 with a blue dashed-dotted line by using $n_H^{6.5\ \text{K}}$ as the effective number of delocalized electrons.

The Korringa mechanism was not only observed in many metals [87], but was also detected in different highly doped semiconductors for high magnetic fields (> 1 T), including Si [98], Ge [99], GaAs [36], and InP [97]. For a higher doped GaAs sample (9×10^{16} cm^{-3}) at low temperatures (< 30 K) and low magnetic fields (< 0.2 mT), the dominant NSR rate indeed is mediated by the Fermi-edge electrons and the NSR rate has a linear relation with the temperature [42].

Although the Korringa mechanism has been observed in many publications [87, 97, 98, 100, 101], other results show deviations from this mechanism. For weak magnetic fields (15 G) and low temperature (< 1 K), a breakdown of the Korringa mechanism and a nonlinear temperature dependence of NSR for temperatures range (0.1 K $\leq T \leq 10$ K) for GaAs was reported [39]. Moreover, there was for example no trace of Korringa in a MIT GaAs sample (2×10^{16} cm^{-3}) at low magnetic fields (< 0.2 mT) using a cavity enhanced Faraday rotation method.

In Fig. 4.11, the measured NSR rate due to diffusion is plotted. This rate is determined by subtracting the Korringa mechanism from the measured NSR rate. As the doping increases above the MIT, the density of localized donors decreases, and according to Eq. 4.29 the NSR rate due to diffusion Γ_D decreases.
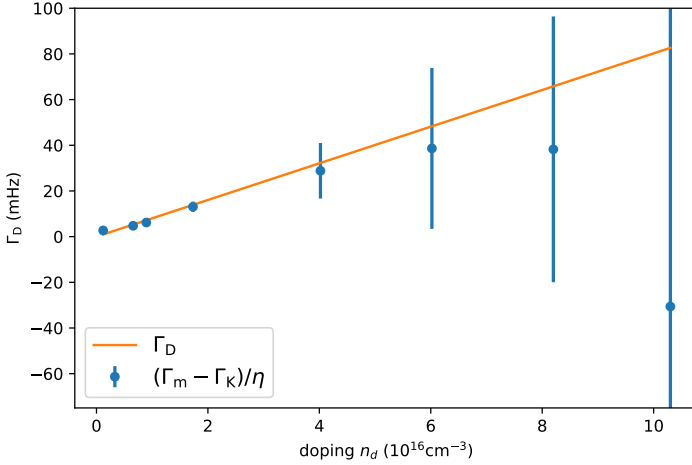

Figure 4.11.: The NSR due to diffusion extracted by subtracting the Korringa rate from the measured relaxation rate (Γ_m) for $T = 6.5$ K and high magnetic field. Above the MIT, the error bars increase significantly since Γ_K becomes much larger than Γ_D.

4.10. Temperature Dependence of the NSR Rate

Figure 4.8 shows an excellent agreement between experiment and theory for all doping densities but the very lowest one, i.e., $n_d = 1.2 \times 10^{15}$ cm^{-3}. In order to bring light into this problem, the temperature dependence of Γ is measured additionally for this low
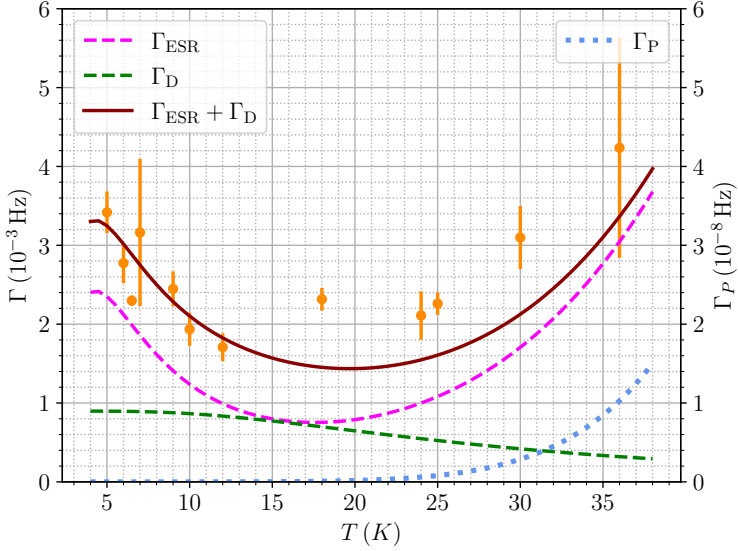
Figure 4.12.: Temperature dependence of Γ for a doping density of $n_d = 1.2 \times 10^{15}$ cm^{-3} measured at high magnetic field. The diffusion mechanism Γ_D is shown as green dashed line. The effect of Γ_{ESR} is shown as pink dashed line. The NSR due to quadrupolar two-phonon process Γ_P is shown with respect to the right axis. Please note that two different scales are used left and right.
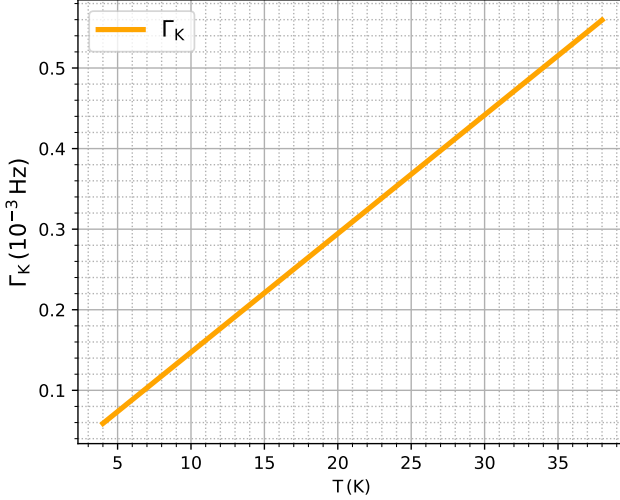
doped sample.

Figure 4.13.: The Korringa mechanism calculated for sample $n_d = 1.2 \times 10^{15}$ cm^{-3} for a temperature range up to 36 K.

The orange dots with error bars in Fig. 4.12 depicts the respective Γ in dependence on temperature. The measured Γ first decreases with increasing temperature but starts to increase at higher temperatures. The error bars are the measured statistical errors only and do not include potential systematic errors. The Korringa mechanism is negligible at such a low doping concentration, as is shown in Fig. 4.13.

As Fig. 4.14 shows, the number of localized electrons is in the low doping sample nearly constant up to 10 K and decreases afterward with increasing temperature. The NSR diffusion mechanism also has the same behavior and decreases continuously with temperature due to thermal ionization of the localized electrons [102]. The green dashed line in Fig. 4.12 depicts the calculated Γ_D, which is significantly too small to explain the experimental data.
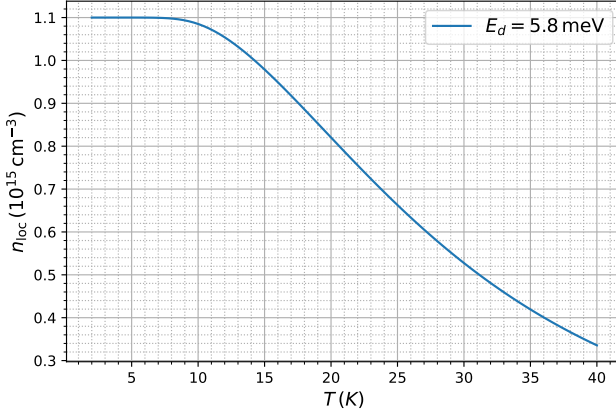
Figure 4.14.: The calculated number of localized carriers in sample S1 is in good approximation constant up to almost 10 K. At higher temperatures, n_{loc} decreases steadily.

One might think that the relatively fast NSR at low temperatures could result from the omnipresent continuous alteration of the local charge environment inducing fluctuating quadrupolar fields. These fields would effectively lead to a relaxation of the nuclear spin system into its equilibrium state [93, 103]. However, firstly the p-type background doping is too small to yield a significant density of charged defects. Secondly, the NSR rate is extracted under dark conditions, i.e., no charge fluctuations due to the above bandgap excitation can take place. All contributions via spin interaction with delocalized electrons type mechanisms do not play a role here since their magnitude is too small in this doping regime. Phonon-induced NSR is another possible involved mechanism in the NSR. However, in the following in subsection 4.10.1, this mechanism is shown to have no effect on the measured temperature dependence of the NSR rate. Basically, the only fluctuating source left radiating into the nuclear spin bath results from the spin relaxation of the localized donor electrons which is explained in subsection 4.10.2.

4.10.1. Phonon-Induced NSR

The coupling between lattice vibrations and the nuclear spins is essential for NSR. The quantum mechanical vibrations are called phonons and generate time-dependent effective magnetic fields or electric-field gradients at the nuclei. These fields induce in turn transitions between energy levels of the nuclear spin system until the nuclear spin polarization reaches thermal equilibrium [87]. Abragam extensively explains the mathematical calculations related to the phonon-induced NSR rate in Ref. [87]. In the following, a short summary of these calculations is provided (see also Ref. [104]).

The effect of phonons on NSR is directly linked to the time-dependent displacement of the nuclei $\mathbf{p}$ from its Bravais lattice $\mathbf{p}a$ at which the position of the nuclei becomes

$$\mathbf{R} = \mathbf{p}a + \mathbf{u}_p, \tag{4.36}$$

where, "a" is the lattice spacing. The displacement vector $\mathbf{u}_p$ can be described in the harmonic approximation that includes absorption and emission of phonons. The total number of phonons "n" present in the crystal at temperature T and frequency ω_p is

$$n = \left[\exp\left(\frac{\hbar\omega_p}{k_B T}\right) - 1\right]^{-1}. \tag{4.37}$$

In order to calculate the transition probabilities induced by the spin-phonon coupling, a coupling Hamiltonian is used:

$$\hbar\mathcal{H}_1 = \hbar F A, \tag{4.38}$$

where $\mathcal{H}_1$ is in frequency units, "A" is the dimensionless spin operator and "F" is the lattice operator with the dimensions of "Hz" and equals

$$F = F_0 + F_1 \mathrm{W} + F_2 \mathrm{W}^2 + ..., \tag{4.39}$$

where $W = \frac{\delta u}{\delta x}$ is the stress. Overall, for the NSR via phonons, two processes are involved:

1. The *Direct process* is related to the emission or absorption of a single phonon while

2. the *Raman process* involves two phonons. One of these two phonons is absorbed, and the other one is emitted.

Based on Eq. 4.39, the *direct process* is related to the term $F_1 W$ and the *Raman process* is determined by $F_2 W^2$. Higher-order terms in Eq. 4.39 have smaller contributions on the relaxation and can be ignored in good approximation.

The relaxation rate between two nuclear spins is[7] for the low temperature case $\hbar\omega_0 \ll k_B T$ and magnetic dipolar coupling

$$ P_1 \sim 9\pi\Omega \left(\frac{F_1}{\Omega} \right)^2 \left(\frac{\omega_0}{\Omega} \right)^2 \left(\frac{k_B \theta_D}{mv^2} \right) \left(\frac{T}{\theta_D} \right) \sim \frac{1}{T_1}, \qquad (4.40) $$

and shows a linear dependence on temperature. Here, $m = (69.723 + 74.921595)$ u is the atomic mass[8] of two atom basis in GaAs and $v = 4.73 \times 10^3$ m/s is the velocity of sound. On the other hand, the relaxation via the *Raman process* is for a magnetic dipolar coupling

$$ P_2 \sim \frac{81\pi}{2} \left(\frac{F_2 \hbar}{mv^2} \right)^2 \int_0^\Omega \frac{e^{\frac{\hbar_\omega}{k_B T}}}{\left(e^{\frac{\hbar_\omega}{k_B T}} - 1 \right)^2} \frac{\omega^6}{\Omega^6} d\omega. \qquad (4.41) $$

There are two possible situations:

$$ P_2 \cong \begin{cases} \frac{81\pi}{2} \left(\frac{F_2 \hbar}{mv^2} \right)^2 \left(\frac{T}{\theta_D} \right)^7 \Omega \left(\frac{16\pi^6}{21} \right), & \text{if } k_B T \ll \hbar\Omega \\ \frac{81\pi}{10} \left(\frac{F_2}{\Omega} \right)^2 \left(\frac{k_B \theta_D}{mv^2} \right)^2 \left(\frac{T}{\theta_D} \right)^2 \Omega, & \text{if } k_B T \gg \hbar\Omega \end{cases} \qquad (4.42) $$

---

[7] $\hbar\omega_0$ is the energy of the emitted or absorbed phonon equals the energy difference between two states.
[8] 1 u = $1.660\,540\,199 \times 10^{-27}$ kg

In the low temperature limit, the NSR rate is proportional to T^7 while for high temperatures, the dependence is proportional to T^2. The same trend for P_1 and P_2 is correct for the quadrupole relaxation by spin-phonon coupling, just the value for $F_1 \sim F_2$ is different:

$$F_1 \sim F_2 = \begin{cases} \dfrac{\mu_0 \gamma_e \gamma_n \hbar}{4\pi r^3}, & \text{for magnetic relaxation} \\ \dfrac{e^2}{\hbar} \dfrac{Q}{4\pi \epsilon_0 \epsilon_r a^3}, & \text{for quadrupole relaxation} \end{cases}$$

where Q is the quadrupole moment, ϵ_r is the relative dielectric constant[9], ϵ_0 is the vacuum dielectric constant, and γ_e and γ_n are the electron and nuclear gyromagnetic ratios, respectively. The free space permeability is μ_0. Figure 4.15 shows the result for *Direct process* and *Raman process* for sample S1.

(a) *Direct process*   (b) *Raman process*
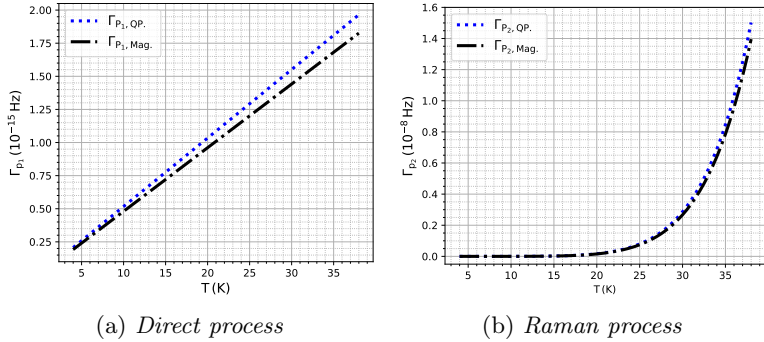
Figure 4.15.: a) P1 from Eq. 4.40 and b) P2 from Eq. 4.42 for both magnetic (Mag) and quadrupolar effect (QP). Note the different scales on the ordinates.

According to the calculations, the experimentally observed increase for $T > 12$ K can not be attributed to the onset of phonon-induced NSR since the impact of dipolar and quadrupolar one-and two-photon contributions is orders of magnitude too small [87]. The

---

[9] In GaAs, $\epsilon_r = 12.35$.

highest NSR rate due to phonons Γ_P relies on quadrupolar two-phonon processes and is shown for the right axis in Fig. 4.12, which differs by five orders of magnitude in comparison to the left axis. Even if these calculations might underestimate Γ_P, comparative measurements from Lu *et al.* [36] on semi-insulating and n-doped GaAs confirm that phonon induced NSR can be neglected at low temperatures in n-doped GaAs.

Phonon-induced relaxation is also observed for $T > 10$ K and $n_d = 5 \times 10^{16}$ cm^{-3} in Ref. [39]. The temperature dependent of the NSR rate is also measured in Ref. [36] which shows the effect of phonon-induced relaxation for high magnetic field $(1 - 13$ T$)$ and $T > 30$ K. In Ref. [105], phonon mediated QP relaxation is the dominant process above 30 K and the rate is proportional to T^2. They measured the temperature dependency for some III-V semiconductors and found out that like in the first measurement on InSb Ref. [106], optical phonons are coupling stronger to III nuclei than to the V nuclei. In Ref. [107], the NSR rate for two isotopes ^{71}Ga and ^{69}Ga are measured. The result shows a linear relation with T up to 250 K. However, for higher temperature the NSR rate is $\propto T^3$. If the sample is doped with magnesium, the two phonon process is observed for $T > 150$ K. In Ref. [97] for $T > 20$ K, the NSR is via two phonon QP effect for ^{69}Ga in samples with $n_d = 2.5 \times 10^{16}$ cm^{-3} and $n_d = 2.1 \times 10^{18}$ cm^{-3}. The role of phonon relaxation is also measured by others Ref. [108, 109].

4.10.2. Electron Effect on the NSR Rate

The only fluctuating source left *radiating* into the nuclear spin bath results from the spin relaxation of the localized donor electrons, which has a distinct temperature dependence due to the joint contribution of spin rotation via HFI and VRH. In the simplest case, these fluctuations should contribute to an additional NSR rate:

$$\Gamma_{ESR} = \mathrm{A}_{\mathrm{ESR}}(\tau_{\mathrm{s,\,HFI}}^{-1} + \tau_{\mathrm{s,\,VRH}}^{-1}), \qquad (4.43)$$

where $\mathrm{A}_{\mathrm{ESR}}$ is a dimensionless coupling constant. The process describes the heat contribution of the localized electron spin dynamics

to the nuclear spin system. The ESR rate in Eq. 4.43 includes VRH and HFI relaxation rates, $\tau_{s,\,VRH}^{-1} + \tau_{s,\,HFI}^{-1}$. The VRH relaxation rate is deduced from Eq. 4.19. The relaxation rate from the HFI is calculated via Eq. 4.26. The sum of two calculated rates of $\Gamma_{ESR} + \Gamma_D$ yields a good agreement with the measured NSR.

Figure 4.12 shows Γ_{ESR} as a dashed magenta line with $A_{ESR} \cong 6.7 \times 10^{-10}$ being the only fitting parameter. The magnitude of the phenomenological coupling constant is mainly given by the considerable difference between the nuclear and the electron spin dephasing rate. The corresponding ESR rate has been calculated according to the values and equations given in Ref. [27]. Please note that Γ_{ESR} has thereby implicitly a dependence on the doping density via the ESR rate's doping density dependence. This context has not been included in the calculated density dependence shown in Fig. 4.8 since (a) the ESR rate and especially the effect of HFI and (b) the fraction of localized electrons decreases significantly with increasing doping concentrations.

Molecular beam epitaxy samples with carrier densities of $n_d = 1.2 \times 10^{15}$ cm^{-3} and lower have not only a finite unintentional carbon background doping concentration but they might also have other unintentional side effects like, for example, electric fields, electron depletion or free electrons from under- or overcompensation of the surface Fermi level pinning. A quantitative study of this process is beyond this thesis's scope. In fact, the observed correlation between Γ and ESR rate might also be coincidental.

5. Conclusion & Outlook

This dissertation presents the electron and the nuclear spin relaxation rates in a contiguous set of accurately characterized n-type GaAs samples, which covers a broad regime of nominal doping densities from quasi-insulating over the Mott metal-to-insulator transition (MIT) up to the degenerate regime. The rates were measured by Hanle depolarization of photoluminescence (PL) in a transverse magnetic field. First, the width of the Lorentzian Hanle curve was used to measure the electron spin relaxation (ESR) rate. The measurements in combination with a theoretical analysis yield a precise insight into the microscopic mechanisms which contribute to the temperature and doping dependences of the ESR rate. The temperature dependence of the ESR rate in the sample with a doping density just below the MIT even shows a non-monotonic dependence, such that the lowest ESR rate was found to be at ~ 7 K in this sample. This minimal rate does not occur at zero but at a finite temperature since the dominating ESR mechanisms based on variable range hopping (VRH) and hyperfine interaction (HFI) have opposite temperature dependencies. For the samples at and above the MIT, the effect of the VRH and the HFI was either small or even negligible, and the Dyakonov Perel (DP) mechanism dominated at all temperatures at which the DP mechanism shows in the highest doped sample a clear transition from degenerate to non-degenerate DP with increasing temperature. At high temperatures, the DP mechanism dominates in all samples, as expected.

The electron and the nuclear spin systems are coupled via HFI. Therefore, the electron spin polarization affects the nuclear spins and results under appropriate conditions in a nuclear spin polarization. This nuclear spin polarization induces a shift and a shape change of the ordinary Hanle curve which enables the measurement

of the nuclear spin relaxation (NSR) dynamics. The NSR rate was measured with a special three-stage protocol. In this method, the system is first optically pumped. Subsequently, the difference of the nuclear spin polarization before and after a dark interval was determined, which enabled measuring the NSR without perturbation by excitation light. The NSR rate decreased in all measured samples with increasing magnetic field. For fields stronger than the local field B_L, the main relaxation mechanism is the nuclear spin diffusion towards donor centers. On the contrary, for lower magnetic fields, the relaxation rate was enhanced due to spin-spin interaction. The increase of the local magnetic field with doping density, is in good approximation within the range of previously published values from the literature. The doping dependence of the NSR rate was measured in the strong field limit at a temperature of 6.5 K. The extracted data shows that the NSR rate increases monotonically with increasing doping density and reaches a maximum at the MIT. The available high precision transport data, including the effective number of localized electrons in each sample at 6.5 K, allowed the quantitative calculation of the NSR rate. The calculation yields an excellent agreement between experiment and theory and provided a clear understanding of the involved NSR mechanisms, considering only nuclear spin diffusion to the donor electrons as efficient killing centers and Korringa spin relaxation from HFI with free electrons. In fact, the spin diffusion constant was the sole, adjustable parameter in these calculations.

Only the measured NSR rate of the very lowest doped sample shows a significant deviation from this quantitative model. Temperature dependent measurements of this sample supported that the effect of the Korringa mechanism was negligible. In addition, the *p*-type background doping was much too small in this lowest doped sample in order to a) yield a significant density of charged defects and b) affect the NSR rate. In other words, fluctuating quadrupolar fields played no significant role in NSR rate of this sample. The probable cause was a nuclear spin heating process by localized electrons with fast HF-induced ESR. Remarkably, the effect of this channel on NSR rate was negligible at high doping

densities. Further experiments and theory are necessary to validate this picture which was not within the scope of this thesis and should be addressed in future experiments.

In general, the thesis provides *inter alia* a quantitative understanding of the ESR rate and the NSR rate in n-doped bulk GaAs. This understanding could be the basics for future experiments on other doped bulk GaAs samples.

On the one hand, the doping type of the sample should be considered. Some co-doping is unavoidable in molecular beam epitaxy grown GaAs due to the presence of p-type carbon impurities. It should be noted that, the co-doping was so small in the measured high-quality samples in this thesis that it didn't play any role in either spin polarization or relaxation dynamics. However, samples with higher co-doping densities are expected to affect both electron and nuclear spin relaxation dynamics. In this case, more ionized impurities are in the system, and momentum scattering time increases. Therefore, motional narrowing is more effective. The DP mechanism will be the dominant relaxation mechanism and as a result, the ESR rate increases. At the same time, the charged impurities result in an electric field and affect the ESR rate. The quadrupole interaction is zero in zinc blend structures in general. However, if the GaAs sample is co-doped, there could be quadrupolar effects from a fluctuating electric field that affects the spins. Much faster ESR is also expected in p-GaAs due to the exchange interaction with holes bound to the acceptors, is more effective. Furthermore, a higher value for the local field and a longer NSR are expected. Interestingly, the effect of quadrupole could be as well strongly strain-dependent inherent to microstructures. Therefore, the strain-induced quadrupole splitting between nuclear spin states could affect the NSR rate. This effect has already been measured in microstructure GaAs samples and semiconductor quantum dots [52] which emphasizes that crucial attention should be paid to the structure of the samples while measuring the NSR rate.

On the other hand, in this thesis, all of the measured GaAs samples were doped with Si with a binding energy of 5.8 meV. In these samples, more ionized impurities can be found for higher tempera-

ture and/or higher doping. However, if the GaAs sample is doped with higher binding energy impurities, the effective Bohr radius is lower. The impurities are more localized, less free electrons are in the valence band, and a higher excitation energy is needed. The result would be lower electron spin polarization, and in turn, the nuclear spin polarization will be also affected via the HFI. Besides, the maximum ESR time for samples below the MIT. This might result in a higher temperature of the minimum ESR compared to the result of this thesis which was at ~ 7 K for the sample just below the MIT.

Appendices

A. Additional Information on the Samples

The structure of the set of n-type GaAs samples measured in this thesis is shown schematically in Fig. A.1, which is besides the doping density in principle the same for all of them. The GaAs substrate is followed by a 500 nm buffer layer and a thick superlattice of alternately layered GaAs and $Al_{0.3}Ga_{0.7}As$ in order to reduce the number of defects and unintentional impurities. The latter has no effect on the optical measurements due to the larger bandgap of the superlattice relative to bulk GaAs. The samples also have two capping layers with 10nm thickness and high doping concentration of $n_d = 4 \times 10^{18}$ cm^{-3} and $n_d = 5 \times 10^{16}$ cm^{-3}, respectively on top and bottom of the epilayer of interest. The high doping of these two layers avoids depletion. For the low doped samples (S1-S5), an extra (AlGa)As capping layer of $n_d = 1 \times 10^{17}$ cm^{-3} reduces any effect from the surface. The epilayer has a 2 μm thickness and different nominal doping densities as $n_d = X \times 10^{16}$ cm^{-3} where $X = 2, 4, 6, 8, 10$, i.e., the doping ranges from the insulating to the metallic regime including the MIT of GaAs ($n_d = 2 \times 10^{16}$ cm^{-3}). The doping densities are quantified by precise high temperature Hall measurements [27] for all studied samples and are summarized in Tab. 3.1.

Figure A.1.: Schematic structure of the samples. The red arrow indicates the growth direction "z". The doping density of the epilayer is a factor ($X \times 10^{16}$ cm^{-3}) and ranges from the insulating into the metallic regime (see Tab. 3.1).

B. Additional Information on the Hanle Calculations

The Hanle effect is based on the degree of circular polarization of the light emitted by the recombining electrons and holes. The degree of circular polarization of the luminescence equals the average electron spin **S** along the observation direction **n**:

$$\rho = -\mathbf{S} \cdot \mathbf{n}. \tag{B.1}$$

The equation of motion for spins in an external magnetic field B including the electron spin lifetime is in steady state [31, 48, 50]

$$\frac{dS}{dt} = \Omega \times S - \frac{S}{\tau_s} - \frac{S}{\tau_r} + \frac{S_0}{\tau_r}. \tag{B.2}$$

Here, S is the time-dependent spin orientation, $\Omega \times S$ the spin precession, Ω the precession frequency, τ_s the spin relaxation time, $\frac{S}{\tau_r}$ the spin relaxation due to radiative recombination of the conduction and the impurity band electrons, and $\frac{S_0}{\tau_r}$ the spin generation rate. The stationary case ($\frac{dS}{dt} = 0$) yields for zero external magnetic field

$$S = S_z(0) = \frac{S_0}{1 + \frac{\tau_r}{\tau_s}}. \tag{B.3}$$

In the case where the external magnetic field is perpendicular to the excitation direction (Voigt geometry), the component of the spin in the z-direction for a given magnetic field and time is

$$S_z(B,t) = S_0 e^{-t/\tau_s} \cos(\Omega t). \tag{B.4}$$

The average measured value of $S_z(B)$ is hence given by

$$S_z(B) = S_0 \int_0^\infty \frac{1}{\tau_r} e^{-t/\tau_r} \cos(\Omega t) e^{-t/\tau_s} dt, \qquad \text{(B.5)}$$

$$S_z(B) = \frac{S_z(0)}{1 + (\Omega T_s)^2} = \frac{S_z(0)}{1 + (g_e \mu_B B_{\text{ext}} T_s/\hbar)^2},$$

where the electron spin lifetime is given as

$$\frac{1}{T_S} = \frac{1}{\tau_S} + \frac{1}{\tau_r}. \qquad \text{(B.6)}$$

The HWHM of the corresponding Lorentz curve (as shown in Fig. 3.1) is

$$B_{\text{HWHM}} = \hbar/g_e \mu_B T_s, \qquad \text{(B.7)}$$

and allows measuring the intrinsic spin relaxation time by extrapolating intensity dependent measurement to zero excitation where the effective τ_r is infinity and $\frac{1}{\tau_r}$ is zero, as explained in subsection 3.2.3.

C. Summary of the Hall Measurements

In order to explain the optical measurement regarding the ESR and the NSR *quantitatively*, the results from the Hall transport measurement are used. The Hall measurements have been carried out in Ref. [10] on the same samples used in this thesis. With these measurements, parameters such as the number of localized electrons, the charge carrier concentration n_H, and the number of electrons in the conduction band n_{cb}, are obtained. In addition, the measured temperature-dependent conductivity helps to find the correlation time τ_c, thereby explaining the involved spin relaxation mechanisms. In the following, a summary of the Hall measurements is provided. More details and results are explained in Ref. [10].

For each sample, an excitation current of $I = 500$ nA is sent through a Hall bar of width W, length L, and depth $d = 2$ μm, so that $\frac{L}{W} = 1.5$. Two voltages for transverse and longitudinal components can be measured. The transverse (Hall) voltage is

$$V_{xy} = R_H \frac{I \cdot B_z}{d}, \tag{C.1}$$

with the Hall constant R_H. The Hall carrier density is the inverse of the measured Hall resistance $n_H = \frac{1}{eR_H}$. The longitudinal voltage is:

$$V_{xx} = \frac{I}{\sigma} \frac{L}{W \cdot d}, \tag{C.2}$$

where σ is the Hall conductivity and is used to derive the Hall mobility $\mu = \frac{\sigma}{ne}$. The momentum relaxation rate is $\frac{1}{\tau_p} = \frac{e}{\mu m_e^*}$.

Figure C.1 shows the temperature dependent of the charge car-
rier concentration determined from the Hall resistance for sample
S1, S3, S6, and S10. The higher temperature part of conductivity
(red fit) gives the Hall densities at room temperature, which yields
the doping density in the high-temperature limit. In fact, at room
temperature, all curves approximate the donor concentration. The
doping from the high temperature fit is considered as a fixed pa-
rameter to fit the low temperature part of Fig. C.1 (green fit) and
find out the relevant parameters which are summarized in Tab. 4.1.
For more information on the fit functions, please see Ref. [10].
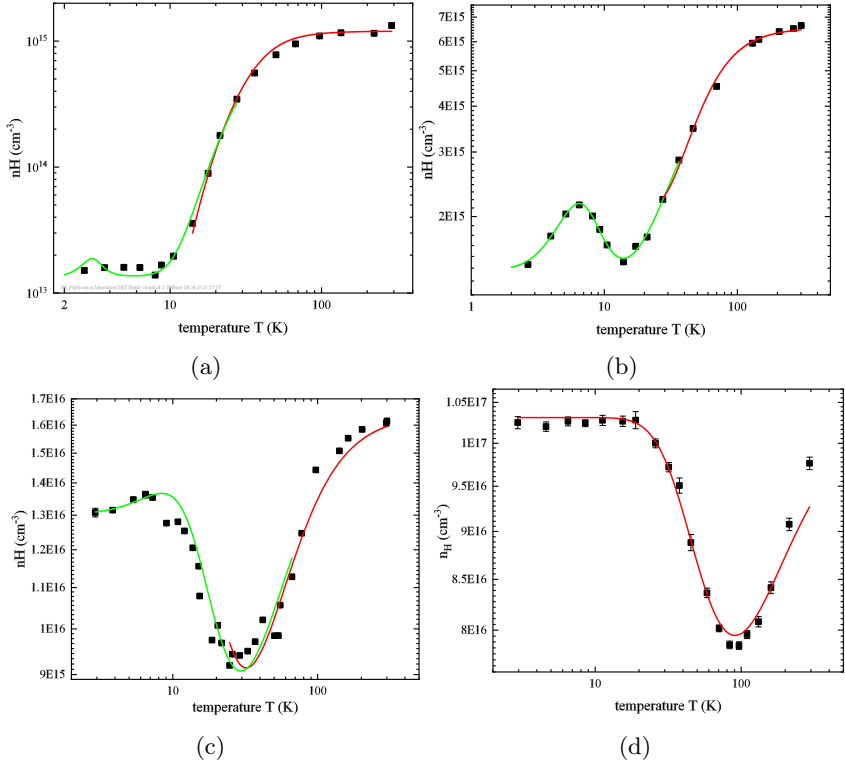
Figure C.1.: Measured doping density for samples a) S1, b) S3, c) S6, and d) S10 in dependence of temperature. These measurements were performed in Ref. [10].

(a) (b)

(c) (d)
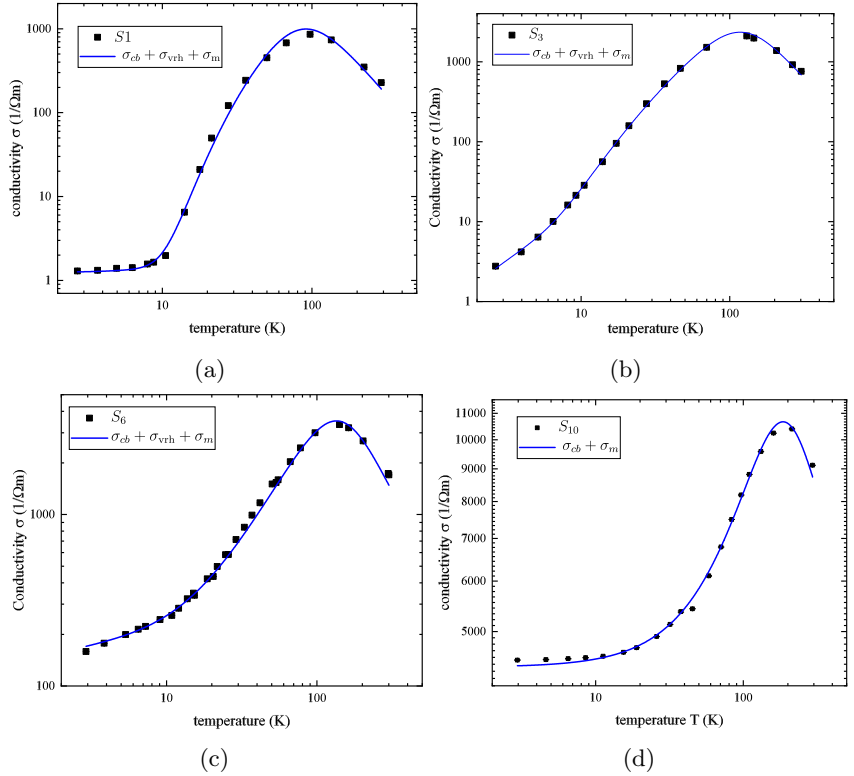
Figure C.2.: Conductivity for samples a) S1, b) S3, c) S6, and d) S10 in dependence of temperature. These measurements were performed in Ref. [10].

D. Additional Information on the DP Mechanism

The bulk inversion asymmetry is important for free electrons in zinc-blende semiconductors like GaAs. The inversion asymmetry of GaAs results from the presence of two different atoms in the Bravais lattice giving rise to a spin splitting, which is proportional to the projection of the spin on the angular momentum: $\Delta E \propto \mathbf{S} \cdot \mathbf{L}$. The SOI is responsible for optical spin orientation, detection, and relaxation. This spin splitting can be described by a $\mathbf{k}$-dependent[1] magnetic field $\mathbf{B(k)}$ which applies a torque on the electron spin magnetic dipole moment with Larmor frequency[2]

$$\mathbf{\Omega(k)} = (e/m)\mathbf{B(k)}. \tag{D.1}$$

The corresponding Hamiltonian for electron precession in the conduction band and the related energy are [6]:

$$\mathcal{H}(\mathbf{k}) = \frac{\hbar}{2}\boldsymbol{\sigma} \cdot \mathbf{\Omega(k)}, \tag{D.2}$$

$$\Delta E = 2\gamma_D \mathrm{k}^3,$$

where $\boldsymbol{\sigma}$ is the spin Pauli operator and γ_D is the Dresselhaus constant.

An important consequence of this $\mathbf{k}$-dependent electron precession in the intrinsic $\mathbf{k}$-dependent magnetic field is the well-known DP spin relaxation mechanism (Eq. 4.2) [78, 79]. An illustration of this

---

[1]$\mathbf{k}$ is the crystal momentum.
[2]The Larmor frequency follows time-reversal symmetry ($\mathbf{\Omega(k)} = -\mathbf{\Omega(k)}$).
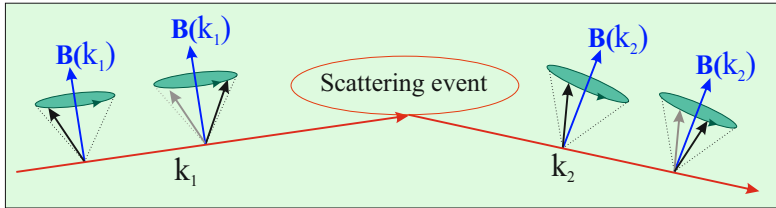
Figure D.1.: Schematic illustration of the DP spin relaxation: A momentum dependent magnetic field (blue arrows) is induced by the SOI around which the electron spin (black arrows) precesses. After each scattering event, the direction of the magnetic field changes accordingly. In this way, the spin relaxation is suppressed by frequent momentum scattering processes.

mechanism is shown in Fig. D.1. As far as the electron moves with $\mathbf{k}_1$, the direction of the effective magnetic field is fixed. After a scattering process, an electron moves with a $\mathbf{k}_2$ which is unequal to $\mathbf{k}_1$ and therefore linked to a different effective magnetic field. Each single scattering event does not make a significant change of the spin orientation if the momentum scattering time is short in comparison to the Larmor precession period. This regime of fast τ_p is called motional narrowing. In fact, the spin dephasing is slow in the motional narrowing regime if the momentum relaxation is fast.

E. Additional Information on the VRH Mechanism

The conductivity in low doped semiconductors and/or at low temperatures mainly depends on different factors: (a) available free states, (b) the distance R_{ij} between donors, and (c) the energy difference between the first and final state. This conductivity is actually due to hopping from an impurity located at cite "i" to another at cite "j". The shorter the distance between these two impurities, the more likely this hopping will occur, i.e., electrons are no longer bound to just one donor. The interaction between the donors increases with doping density and broadens the density of states. However, for tunneling the energy difference between two cites has to be $E_{ij} \leq k_B T$. This second factor is opposite to the first factor and indicates an increase in hopping probability by decreasing the distance. Competition between these two factors causes an optimal distance. The resulting optimal hopping distance depends on the temperature and the thermal energy available. During this hopping, VRH spin relaxation mechanism happens. For further details, see Ref. [10].

Bibliography

[1] G. E. Moore, "Cramming more components onto integrated circuits", Proceedings of the IEEE **86**, 82 (1998).

[2] M. M. Waldrop, "The chips are down for Moore's law", Nature News **530**, 144 (2016).

[3] M. I. D'yakonov, *Will We Ever Have a Quantum Computer?*, Springer, 2020.

[4] C. H. Bennett, "Quantum information and computation", Physics Today **48**, 24 (1995).

[5] R. Jansen, "Silicon spintronics", Nature materials **11**, 400 (2012).

[6] I. Žutić, J. Fabian, and S. D. Sarma, "Spintronics: Fundamentals and applications", Reviews of modern physics **76**, 323 (2004).

[7] W. Witzel and S. D. Sarma, "Nuclear spins as quantum memory in semiconductor nanostructures", Phys. Rev. B **76**, 045218 (2007).

[8] J. J. Morton, A. M. Tyryshkin, R. M. Brown, S. Shankar, B. W. Lovett, A. Ardavan, T. Schenkel, E. E. Haller, J. W. Ager, and S. Lyon, "Solid state quantum memory using the 31P nuclear spin", Nature **455**, 1085 (2008).

[9] J. Taylor, C. Marcus, and M. Lukin, "Long-lived memory for mesoscopic quantum bits", Phys. Rev. Lett. **90**, 206803 (2003).

[10] J. G. Lonnemann, "Einfluss der Ladungsträgerdynamik auf die Spinrelaxation in GaAs", PhD thesis, Hannover: Gottfried Wilhelm Leibniz Universität Hannover, 2017.

[11] M. D'yakonov and V. Perel, "Spin orientation of electrons associated with the interband absorption of light in semiconductors", JETP **33**, 1053 (1971).

[12] M. D'yakonov and V. Perel, "Feasibility of optical orientation of equilibrium electrons in semiconductors", JETP **13**, 144 (1971).

[13] C. Hermann, G. Lampel, and V. Safarov, "Optical pumping in semiconductors", Annales de Physique **10**, 1117 (1985).

[14] G. Lampel, "Nuclear dynamic polarization by optical electronic saturation and optical pumping in semiconductors", Phys. Rev. Lett. **20**, 491 (1968).

[15] R. Parsons, "Band-to-band optical pumping in solids and polarized photoluminescence", Phys. Rev. Lett. **23**, 1152 (1969).

[16] A. Ekimov and V. Safarov, "Optical orientation of carriers in interband transitions in semiconductors", JETP **12**, 1 (1970).

[17] B. Zakharchenya, V. Fleisher, R. Dzhioev, Y. P. Veshchunov, and I. Rusanov, "Effect of optical orientation of electron spins in a GaAs crystal", J. Exp. Theor. Phys. Lett. **13**, 195 (1971).

[18] A. Ekimov and V. Safarov, "Observation of optical orientation of equilibrium electrons in n-type semiconductors", JETP **13**, 177 (1971).

[19] R. Dzhioev, B. Zakharchenya, V. Korenev, and M. Stepanova, "Spin diffusion of optically oriented electrons and photon entrainment in n-gallium arsenide", Physics of the Solid State **39**, 1765 (1997).

[20] W. Hanle, "Über magnetische beeinflussung der polarisation der resonanzfluoreszenz", Zeitschrift für Physik **30**, 93 (1924).

[21] J. Brossel and A. Kastler, "Magnetic Resonance Detection Of Excited Levels-The Effect Of Depolarization Of Optical Resonance And Fluorescence Radiation", Weekly Reports Of Seances De L Academie Des Sciences **229**, 1213 (1949).

[22] J. Kikkawa and D. Awschalom, "Resonant spin amplification in n-type GaAs", Phys. Rev. Lett. **80**, 4313 (1998).

[23] J. Kikkawa and D. Awschalom, "Lateral drag of spin coherence in gallium arsenide", Nature **397**, 139 (1999).

[24] S. A. Crooker, L. Cheng, and D. L. Smith, "Spin noise of conduction electrons in n-type bulk GaAs", Phys. Rev. B **79**, 035208 (2009).

[25] R. Dzhioev, K. Kavokin, V. Korenev, M. Lazarev, B. Y. Meltser, M. Stepanova, B. Zakharchenya, D. Gammon, and D. Katzer, "Low-temperature spin relaxation in n-type GaAs", Phys. Rev. B **66**, 245204 (2002).

[26] K. Kavokin, "Spin relaxation of localized electrons in n-type semiconductors", Semiconductor Science and Technology **23**, 114009 (2008).

[27] J. G. Lonnemann, E. P. Rugeramigabo, M. Oestreich, and J. Hübner, "Closing the gap between spatial and spin dynamics of electrons at the metal-to-insulator transition", Phys. Rev. B **96**, 045201 (2017).

[28] W. D. Knight, "Nuclear magnetic resonance shift in metals", Phys. Rev. **76**, 1259 (1949).

[29] M. D'yakonov and V. Perel, "Optical orientation in a system of electrons and lattice nuclei in semiconductors. Theory", Zh. Eksp. Teor. Fiz **65**, 362 (1973).

[30] V. Berkovits, A. Ekimov, and V. Safarov, "Optical Orientation in a System of Electrons and Lattice Nuclei in Semiconductors-Experiment", Zh. Eksp. Teor. Fiz **65**, 346 (1973).

[31] F. Meier and B. P. Zakharchenya, *Optical Orientation*, Elsevier, 2012.

[32] A. Ekimov and V. Safarov, "Optical electron-nuclear resonance in semiconductors", J. Exp. Theor. Phys. Lett. **15**, 453 (1972).

[33] A. W. Overhauser, "Polarization of nuclei in metals", Phys. Rev. **92**, 411 (1953).

[34] D. Paget, G. Lampel, B. Sapoval, and V. Safarov, "Low field electron-nuclear spin coupling in gallium arsenide under optical pumping conditions", Phys. Rev. B **15**, 5780 (1977).

[35] D. Paget, "Optical detection of NMR in high-purity GaAs: Direct study of the relaxation of nuclei close to shallow donors", Phys. Rev. B **25**, 4444 (1982).

[36] J. Lu, M. Hoch, P. Kuhns, W. Moulton, Z. Gan, and A. Reyes, "Nuclear spin-lattice relaxation in n-type insulating and metallic GaAs single crystals", Phys. Rev. B **74**, 125208 (2006).

[37] J. Huang, Y. Chen, A. Ludwig, D. Reuter, A. Wieck, and G. Bacher, "Electron-nuclei spin coupling in GaAs: Free versus localized electrons", Appl. Phys. Lett. **100**, 132103 (2012).

[38] J. Korringa, "Nuclear magnetic relaxation and resonnance line shift in metals", Physica **16**, 601 (1950).

[39] D. Kölbl, D. M. Zumbühl, A. Fuhrer, G. Salis, and S. F. Alvarado, "Breakdown of the Korringa law of nuclear spin relaxation in metallic GaAs", Phys. Rev. Lett. **109**, 086601 (2012).

[40] I. Merkulov, "Nuclear field and faraday effect in semiconductors", Fizika Tverdogo Tela **27**, 1558 (1985).

[41] R. Giri, "Electron and nuclear spin dynamics in GaAs micro-cavities", PhD thesis, Université Montpellier II-Sciences et Techniques du Languedoc, 2013.

[42] M. Kotur, R. Dzhioev, K. Kavokin, V. L. Korenev, B. Namozov, P. Pak, and Y. G. Kusrayev, "Nuclear spin relaxation mediated by Fermi-edge electrons in n-type GaAs", JETP **99**, 37 (2014).

[43] I. Ryzhov et al., "Measurements of nuclear spin dynamics by spin-noise spectroscopy", App. Phys. Lett. **106**, 242405 (2015).

[44] M. Vladimirova, S. Cronenberger, D. Scalbert, M. Kotur, R. Dzhioev, I. Ryzhov, G. Kozlov, V. Zapasskii, A. Lemaître, and K. Kavokin, "Nuclear spin relaxation in n-GaAs: From insulating to metallic regime", Phys. Rev. B **95**, 125312 (2017).

[45] V. Litvyak, R. Cherbunin, K. Kavokin, and V. Kalevich, "Determination of the local field in the nuclear spin system of n-type GaAs", Journal of Physics: Conference Series **951**, 012006 (2018).

[46] P. Sokolov, M. Y. Petrov, K. Kavokin, M. Kuznetsova, S. Y. Verbin, I. Y. Gerlovin, D. Yakovlev, and M. Bayer, "Subsecond nuclear spin dynamics in n-GaAs", Phys. Rev. B **99**, 075307 (2019).

[47] P. Sokolov et al., "Nuclear spin cooling by helicity-alternated optical pumping at weak magnetic fields in n-GaAs", Phys. Rev. B **96**, 205205 (2017).

[48] M. I. D'yakonov and A. Khaetskii, *Spin physics in semiconductors*, Springer, 2017.

[49] R. K. Harris, E. D. Becker, S. M. C. De Menezes, R. Goodfellow, and P. Granger, "NMR nomenclature. Nuclear spin

properties and conventions for chemical shifts (IUPAC Recommendations 2001)", Pure and Applied Chemistry **73**, 1795 (2001).

[50] M. M. Glazov, *Electron & Nuclear Spin Dynamics in Semiconductor Nanostructures*, Oxford University Press, 2018.

[51] C. H. Wang, *Spectroscopy of condensed media: dynamics of molecular interactions*, Elsevier, 2012.

[52] B. Urbaszek, X. Marie, T. Amand, O. Krebs, P. Voisin, P. Maletinsky, A. Högele, and A. Imamoglu, "Nuclear spin physics in quantum dots: An optical investigation", Reviews of Modern Physics **85**, 79 (2013).

[53] M. Goldman, *spin temperature and nuclear magnetic resonance in solids*, Oxford Univ. Press (Clarendon), London and New York, 1970.

[54] E. M. Lifshitz and L. P. Pitaevskii, *Statistical physics: theory of the condensed state*, Elsevier, 2013.

[55] E. M. Purcell and R. V. Pound, "A nuclear spin system at negative temperature", Phys. Rev. **81**, 279 (1951).

[56] N. Bloembergen, "On the interaction of nuclear spins in a crystalline lattice", Physica **15**, 386 (1949).

[57] R. Pound, "Nuclear electric quadrupole interactions in crystals", Phys. Rev. **79**, 685 (1950).

[58] R. Dzhioev, I. Aksyanov, M. Lazarev, and O. Ninua, "Study of the Hanle effect with the transverse component of the electron spin orientation in III–V semiconductors", Physics of the Solid State **48**, 2270 (2006).

[59] F. Bloch, "Nuclear induction", Phys. Rev. **70**, 460 (1946).

[60] D. Pines and C. P. Slichter, "Relaxation times in magnetic resonance", Phys. Rev. **100**, 1014 (1955).

[61] R. K. Wangsness and F. Bloch, "The dynamical theory of nuclear induction", Phys. Rev. **89**, 728 (1953).

[62] F. Heisterkamp, E. Zhukov, A. Greilich, D. Yakovlev, V. Korenev, A. Pawlis, and M. Bayer, "Longitudinal and transverse spin dynamics of donor-bound electrons in fluorine-doped ZnSe: Spin inertia versus Hanle effect", Phys. Rev. B **91**, 235432 (2015).

[63] C. Lü, J. Cheng, M. Wu, and I. da Cunha Lima, "Spin relaxation time, spin dephasing time and ensemble spin dephasing time in n-type GaAs quantum wells", Physics Letters A **365**, 501 (2007).

[64] S. Cronenberger and D. Scalbert, "Quantum limited heterodyne detection of spin noise", Review of Scientific Instruments **87**, 093111 (2016).

[65] V. Kalevich, V. Korenev, and O. Fedorova, "Optical polarization of nuclei in GaAs/AlGaAs quantum-well structures", JETP **52**, 349 (1990).

[66] R. Dzhioev, V. Korenev, I. Merkulov, B. Zakharchenya, D. Gammon, A. L. Efros, and D. Katzer, "Manipulation of the Spin Memory of Electrons in n-GaAs", Phys. Rev. Lett. **88**, 256801 (2002).

[67] M. D'yakonov, V. Perel, V. Berkovits, and V. Safarov, "Optical effects due to polarization of nuclei in semiconductors", JETP **40**, 950 (1975).

[68] V. Kalevich, V. Kulkov, and V. Fleisher, "Optical cooling of the nuclear spin system of a semiconductor in a conjunction with the adiabatic demagnetization", Bull. Acad. Sci. USSR, Phys. Ser **46**, 70 (1982).

[69] M. Römer, H. Bernien, G. Müller, D. Schuh, J. Hübner, and M. Oestreich, "Electron-spin relaxation in bulk GaAs for doping densities close to the metal-to-insulator transition", Phys. Rev. B **81**, 075216 (2010).

[70] S. Oertel, J. Huebner, and M. Oestreich, "High temperature electron spin relaxation in bulk GaAs", App. Phys. Lett. **93**, 132112 (2008).

[71] J. Jiang and M. Wu, "Electron-spin relaxation in bulk III-V semiconductors from a fully microscopic kinetic spin Bloch equation approach", Phys. Rev. B **79**, 125206 (2009).

[72] J. Colton, T. Kennedy, A. Bracker, and D. Gammon, "Spin Lifetime Measurements in MBE-Grown GaAs Epilayers", physica status solidi (b) **233**, 445 (2002).

[73] J. S. Colton, M. Heeb, P. Schroeder, A. Stokes, L. Wienkes, and A. Bracker, "Anomalous magnetic field dependence of the T 1 spin lifetime in a lightly doped GaAs sample", Phys. Rev. B **75**, 205201 (2007).

[74] R. Dzhioev, B. P. Zakharchenya, V. L. Korenev, D. Gammon, and S. Katzer, "Long electron spin memory times in gallium arsenide", J. Exp. Theor. Phys. **74**, 182 (2001).

[75] K. Kavokin, "Anisotropic exchange interaction of localized conduction-band electrons in semiconductors", Phys. Rev. B **64**, 075305 (2001).

[76] J. Kainz, U. Rössler, and R. Winkler, "Temperature dependence of Dyakonov-Perel spin relaxation in zinc-blende semiconductor quantum structures", Phys. Rev. B **70**, 195322 (2004).

[77] M. Wu, J. Jiang, and M. Weng, "Spin dynamics in semiconductors", Physics Reports **493**, 61 (2010).

[78] M. D'yakonov and V. Perel, "Spin relaxation of conduction electrons in noncentrosymmetric semiconductors", Soviet Physics Solid State, Ussr **13**, 3023 (1972).

[79] G. Pikus and A. Titkov, "Spin relaxation under optical orientation in semiconductors", Optical Orientation **8**, 73 (1984).

[80] M. Beck, "Electron spin relaxation, transport and strain-induced precession in n-GaAs", PhD thesis, Erlangen: Lehrstuhl für Mikrochakterisierung, Friedrich-Alexander-Universität, Erlangen, 2005.

[81] H. Ibach and H. Lüth, *Festkörperphysik: Einführung in die Grundlagen*, Springer, 2009.

[82] D. Chattopadhyay and H. Queisser, "Electron scattering by ionized impurities in semiconductors", Rev. Mod. Phys. **53**, 745 (1981).

[83] L. Gorkov and P. Krotkov, "Spin relaxation and antisymmetric exchange in n-doped III-V semiconductors", Phys. Rev. B **67**, 033203 (2003).

[84] J. Hübner, S. Döhrmann, D. Hägele, and M. Oestreich, "Temperature-dependent electron Landé g factor and the interband matrix element of GaAs", Phys. Rev. B **79**, 193307 (2009).

[85] M. Oestreich, S. Hallstein, A. Heberle, K. Eberl, E. Bauser, and W. Rühle, "Temperature and density dependence of the electron Landé g factor in semiconductors", Phys. Rev. B **53**, 7911 (1996).

[86] L. Abaspour, P. Sterin, E. P. Rugeramigabo, J. Hübner, and M. Oestreich, "Doping and temperature dependence of nuclear spin relaxation in *n*-type GaAs", Phys. Rev. B **102**, 235205 (2020).

[87] A. Abragam, *The principles of nuclear magnetism*, Oxford university press, 1961.

[88] A. Oja and O. Lounasmaa, "Nuclear magnetic ordering in simple metals at positive and negative nanokelvin temperatures", Rev. Mod. Phys. **69**, 1 (1997).

[89] M. Kotur, R. Dzhioev, M. Vladimirova, B. Jouault, V. Korenev, and K. Kavokin, "Nuclear spin warm up in bulk n-GaAs", Phys. Rev. B **94**, 081201 (2016).

[90] A. Evdokimov, M. Kuznetsova, M. Y. Petrov, R. Potekhin, Y. P. Efimov, S. Eliseev, V. Lovtcius, and P. Y. Shapochkin, "Strongly-coupled electron and nuclear spin systems in In-GaAs epilayers", Journal of Physics: Conference Series **1199**, 012002 (2019).

[91] M. J. Dominguez, J. R. Iafrate, and V. Sih, "Dynamic nuclear polarization by optical Stark effect in periodically pumped gallium arsenide", Phys. Rev. B **101**, 205203 (2020).

[92] M. Vladimirova, S. Cronenberger, D. Scalbert, I. Ryzhov, V. Zapasskii, G. Kozlov, A. Lemaître, and K. Kavokin, "Spin temperature concept verified by optical magnetometry of nuclear spins", Phys. Rev. B **97**, 041301 (2018).

[93] D. Paget, T. Amand, and J.-P. Korb, "Light-induced nuclear quadrupolar relaxation in semiconductors", Phys. Rev. B **77**, 245201 (2008).

[94] R. Giri, S. Cronenberger, M. Glazov, K. Kavokin, A. Lemaître, J. Bloch, M. Vladimirova, and D. Scalbert, "Nondestructive measurement of nuclear magnetization by off-resonant faraday rotation", Phys. Rev. Lett. **111**, 087603 (2013).

[95] N. Bloembergen, "Nuclear magnetic relaxation in semiconductors", Physica **20**, 1130 (1954).

[96] P. De Gennes, "Sur la relaxation nucleaire dans les cristaux ioniques", Journal of Physics and Chemistry of Solids **7**, 345 (1958).

[97] G. Kaur and G. Denninger, "Dynamic nuclear polarization in III–V semiconductors", Appl. Magn. Reson. **39**, 185 (2010).

[98] R. Sundfors and D. Holcomb, "Nuclear magnetic resonance studies of the metallic transition in doped silicon", Phys. Rev. **136**, A810 (1964).

[99] D. Tunstall and V. Deshmukh, "Conduction electrons in an impurity band: NMR in Ge: As", Journal of Physics C: Solid State Physics **12**, 2295 (1979).

[100] C. P. Slichter, *Principles of magnetic resonance*, Springer Science & Business Media, 2013.

[101] A. Anderson and A. Redfield, "Nuclear spin-lattice relaxation in metals", Phys. Rev. **116**, 583 (1959).

[102] J. S. Blakemore, *Semiconductor statistics*, Courier Corporation, 2002.

[103] M. Kotur, R. Dzhioev, M. Vladimirova, R. Cherbunin, P. Sokolov, D. Yakovlev, M. Bayer, D. Suter, and K. Kavokin, "Spin-lattice relaxation of optically polarized nuclei in p-type GaAs", Phys. Rev. B **97**, 165206 (2018).

[104] J. Dolinšek, P. Cereghetti, and R. Kind, "Phonon-assisted spin diffusion in solids", J. Magn. Reson. **146**, 335 (2000).

[105] J. A. McNeil and W. G. Clark, "Nuclear quadrupolar spin-lattice relaxation in some III-V compounds", Phys. Rev. B **13**, 4705 (1976).

[106] F. Bridges and W. G. Clark, "Quadrupolar Nuclear Spin-Lattice Relaxation in InSb at Low and Medium Temperatures", Phys. Rev. **164**, 288 (1967).

[107] M. Corti, A. Gabetta, M. Fanciulli, A. Svane, and N. Christensen, "69, 71 Ga NMR spectra and relaxation in wurtzite GaN", Phys. Rev. B **67**, 064416 (2003).

[108] J. Van Kranendonk, "Theory of quadrupolar nuclear spin-lattice relaxation", Physica **20**, 781 (1954).

[109] V. Mikushev, A. Ulyashev, E. Charnaya, and A. Chandoul, "Temperature dependence of the spin-lattice relaxation time for quadrupole nuclei under conditions of NMR line saturation", Physics of the Solid State **44**, 1044 (2002).

List of Figures

List of Tables

Curriculum Vitae

Lida Abaspour,
born on February 11th, 1987 in Eslamabad Gharb, Iran

2016-today	Employment as research assistant and preparation of the doctoral thesis at the Institute for Solid State Physics - Nanostructures Group, Leibniz University Hannover, supervised by Prof. Dr. M. Oestreich
2011- 2013	MSc degree in physics, University of Kurdistan (UoK), Iran
2006- 2011	BSc degree in physics, Razi University, Iran
2002 - 2006	High school, Mathematics and physics, Iran
1994 - 2001	Elementary school, Iran

List of Publications

The following list contains authored and co-authored scientific publications which were submitted during the time as a PhD-student:

- **L. Abaspour**, P. Sterin, E. P. Rugeramigabo, J. Hübner, and M. Oestreich, *Temperature dependence of the electron spin relaxation in n-type GaAs*, to be submitted.

- **L. Abaspour**, P. Sterin, E. P. Rugeramigabo, J. Hübner, and M. Oestreich, *Doping and temperature dependence of nuclear spin relaxation in n-type GaAs*, Phys. Rev. B **102**, 235205 (2020).

- J. Wiegand, D. S. Smirnov, J. Osberghaus, **L. Abaspour**, J. Hübner, and M. Oestreich, *Hole-capture competition between a single quantum dot and an ionized acceptor*, Phys. Rev. B **98**, 125426 (2018).

Contributions to Scientific Conferences

The following list contains leading-author contributions to scientific conferences during the time as a PhD student:

- **L. Abaspour**, P. Sterin, J. G. Lonnemann, E. P. Rugeramigabo, J. Hübner, and M. Oestreich, *Nuclear spin dynamics in n-GaAs* (Poster), DPG Spring Meeting of the Condensed Matter Section, Regensburg, Germany (2019).

- **L. Abaspour**, P. Sterin, J. G. Lonnemann, E. P. Rugeramigabo, J. Hübner, and M. Oestreich, *Electron and Nuclear Spin Dynamics in n-type GaAs* (Poster), Workshop of the DFG Research Training Group 1991 (quantum mechanical noise in complex systems), Hannover, Germany (2018).

- **L. Abaspour**, P. Sterin, J. G. Lonnemann, E. P. Rugeramigabo, J. Hübner, and M. Oestreich, *Temperature and doping Dependence of Electron and Nuclear Spin Relaxation Time in n-type GaAs* (Poster), NanoDay of the Laboratory for Nano and Quantum Engineering, Hannover, Germany (2018).

- **L. Abaspour**, J. G. Lonnemann, E. P. Rugeramigabo, J. Hübner, and M. Oestreich, *Doping and Temperature Dependence of Nuclear Spin Relaxation in n-type GaAs* (Poster), Nanotechnology Meets Quantum Information, San Sebastian, Spain (2017).

- **L. Abaspour**, J. G. Lonnemann, E. P. Rugeramigabo, J. Hübner, and M. Oestreich, *Nuclear Spin Relaxation in n-type*

GaAs (Poster), DPG Spring Meeting of the Condensed Matter Section, Dresden, Germany (2017).

Acknowledgements

I would like to appreciate my supervisor Prof. Dr. Michael Oestreich, for giving me the opportunity to do my Ph.D. in his group, which was a giant leap forward in my life. He not only supervised me to fulfill my Ph.D. project and provided the answer to my questions but also how to enjoy my life in Germany. Without his support, learning the German language and the confidence to talk in German was impossible. Accomplishing this dissertation could not be that enjoyable without the help and companion of him and people who should be acknowledged here.

Looking back to the time doing research in a new country, it is clear for me that it was impossible without the help of PD Dr. Jens Hübner. Whenever I had any questions, he was always available and explained me. Even during the Corona pandemic, his virtual office was always free to enter. Many thanks for all your patience and kindness. Moreover, special thanks for all your valuable comments on my thesis. By the way, I will never forget the *birthday congratulation* I got from your children.

I would like to thank Prof. Dr. Ding for being the second examiner, and I thank Prof. Dr. Korn for being the external reviewer of this thesis. Moreover, I thank Prof. Dr. Frahm for heading the examination committee of my defense.

I thank Dr. Jan Gerrit Lonnemann, who supervised me with the first experiments on the NSR and the ESR measurements. I learned a lot from you. Moreover, thanks for your accurate transport measurements on the same samples of my PhD project which was very helpful for the quantitative explanation of my results.

Many thanks to Pavel Sterin, who always helped me in the lab with many helpful experimental tips and in the office with all python errors. I really enjoyed working together on some parts of the ESR

data.

I also thank Dr. Julia Wiegand for teaching me experimental techniques in the LNQE. Thank you very much for being always supportive and encouraging me.

The time that I spent in office 131 with Dr. Hendrik Kuhn, Magnus Neumann, Dr. Julia Wiegand, Dr. Michael Beck, Pavel Sterin, and Tianjiao Sun, I never felt homesick. Thank you guys for all your help, your suggestions on experimental issues, and all the enjoyable moments. I thank Eduard Sauter, Kai Hühn, Andrè Frauendorf, and all the new group members Eric Dunkel, Kevin Rempel, Manuel Amanuel, and Florian Lange for giving me memorable moments.

I thank Ronny Hüther and all the workshop members for all their technical help.

Many thanks to Yvonne, Anna, Klara, and Mirija, who always helped me with the paperwork.

I would like to thank Dr. Eddy Rugeramigabo for providing the high-quality samples for this work.

I am very grateful for "RTG1991" for the financial support of my Ph.D. period and for providing many interesting talks and workshops.

I thank the international office and the Hochschulbüro für ChancenVielfalt of the Leibniz University Hannover for all get-together activities, excursions, a mentoring team, and soft skills seminars from where I found many good friends.

Finally, I thank my parents Kakeh & Mani and the whole family who always respect my choices, encourage me, and support me. I love you and miss all of you.

Finally, but definitely not the least, I thank my love Sadjad to whom my love and longing are beyond words. I have been extremely fortunate to have you in my life. Thank you so much for all your support, encourage, hope and patience. I look forward to our future life and to make all our dreams come true together. By the way, you were the best colleague during the Corona-Pandemic for me.